Commun. Comput. Phys.
doi: 10.4208/cicp.050814.040915a

Vol. **19**, No. 4, pp. 841-880
April 2016

Divergence-Free WENO Reconstruction-Based Finite Volume Scheme for Solving Ideal MHD Equations on Triangular Meshes

Zhiliang Xu[1,*], Dinshaw S. Balsara[2,*] and Huijing Du[3]

[1] *Department of Applied and Computational Mathematics and Statistics, University of Notre Dame, Notre Dame, IN 46556, USA.*
[2] *Department of Physics, University of Notre Dame, Notre Dame, IN 46556, USA.*
[3] *Department of Mathematics, University of California, Irvine, Irvine, CA 92697, USA.*

Communicated by Chi-Wang Shu

Received 5 August 2014; Accepted (in revised version) 4 September 2015

Abstract. In this paper, we introduce a high-order accurate constrained transport type finite volume method to solve ideal magnetohydrodynamic equations on two-dimensional triangular meshes. A new divergence-free WENO-based reconstruction method is developed to maintain exactly divergence-free evolution of the numerical magnetic field. In this formulation, the normal component of the magnetic field at each face of a triangle is reconstructed uniquely and with the desired order of accuracy. Additionally, a new weighted flux interpolation approach is also developed to compute the z-component of the electric field at vertices of grid cells. We also present numerical examples to demonstrate the accuracy and robustness of the proposed scheme.

AMS subject classifications: 65M08, 65Z05, 85-08
Key words: Finite volume method, MHD equations, globally divergence-free.

1 Introduction

The ideal magnetohydrodynamic (MHD) equations model the dynamics of an electrically conducting fluid. Numerical solutions to MHD equations are of great importance to many applications in astrophysics and engineering. Many efforts in solving the ideal MHD equations numerically have focused on the divergence-free evolution of the magnetic field implied by the induction equation

$$\frac{\partial \mathbf{B}}{\partial t} + \nabla \times \mathbf{E} = 0. \tag{1.1}$$

*Corresponding author. *Email addresses:* zxu2@nd.edu (Z. Xu), Dinshaw.S.Balsara.1@nd.edu (D. S. Balsara), huijingd@uci.edu (H. Du)

 ©2016 Global-Science Press

https://doi.org/10.4208/cicp.050814.040915a Published online by Cambridge University Press

Here $\mathbf{B}$ is the magnetic field. $\mathbf{E}$ is the electric field defined by $\mathbf{E}=-\mathbf{u}\times\mathbf{B}$ for the ideal MHD flow. $\mathbf{u}$ is the velocity, and $\mathbf{J}=\nabla\times\mathbf{B}$ is the current density. The induction equation implies that the magnetic field remains divergence-free if it is divergence-free initially. In numerical simulations, maintaining discrete divergence-free is also important. Previous studies [8, 15] have shown that a divergence error on the order of numerical truncation error introduced by the numerical scheme can lead to spurious solutions and the production of negative pressures. Recent work by [47, 48] has shown that positivity can be preserved in MHD simulations. Nevertheless, the magnitude of the divergence error could depend on numerical schemes. For instance, the central scheme shows smaller divergence error than the upwind-type schemes [2, 3]. Recent work in [30] showed that the central scheme on overlapping cells and without using constraint transport (CT) formulation to satisfy divergence-free constraint also works for certain test problems. However, Results obtained by the central scheme without using CT formulation shows relatively large divergence error for blast wave and rotor test problems compared with these obtained by using CT formulation.

To name a few methods to ensure divergence-free evolution of the magnetic field, these include Hodge projection approach [45], Powell's source term formulation [34], locally divergence-free discontinuous Galerkin (DG) method [18, 29], CT methods [4, 5, 7, 16, 19, 23, 36, 37, 44], generalized Lagrange Multiplier method [20], and many others [15, 28, 42].

Despite these advances, almost all previous works have been focused on rectangular meshes. The CT type divergence-free formulation on rectangular meshes has been achieved at the second-order accuracy in [6, 7] and higher order of accuracy in [10]. Several problems with complex geometry require the use of triangular meshes. It is, therefore, desirable to design high-order accurate schemes possessing a globally divergence-free property for solving ideal MHD equations on unstructured meshes.

For schemes using CT type formulation on rectangular meshes, the second-order accurate representation of the magnetic field at the cell center can always be obtained by averaging the facial magnetic field. However, on the triangular meshes, this is not so straightforward, as there is no concept of arithmetic averaging of facial magnetic field to the center of the grid cells. As a result, the zone averaged magnetic field has always to be obtained via a reconstruction process on triangular meshes. This makes divergence-free formulation of schemes to solve ideal MHD equations on triangular meshes slightly more intricate than the same process on rectangular meshes.

In this paper, we introduce a divergence-free WENO reconstruction-based finite volume scheme up to the third-order accuracy for solving ideal MHD equations on two-dimensional triangular meshes. ENO and WENO finite volume schemes have been introduced in many previous works for solving scalar conservation laws as well as compressible hydrodynamical flow problems using unstructured meshes [1, 21, 24–26, 26, 41]. However, to the best of our knowledge, globally divergence-free high-order (>2) accurate finite volume schemes for solving ideal MHD equations on triangular meshes have not yet been available. To satisfy the divergence-free constraint on the magnetic field, we

https://doi.org/10.4208/cicp.050814.040915a Published online by Cambridge University Press

employ the CT framework. The basic idea of the CT framework adopted in the present paper is to introduce a staggered magnetic field on cell edges in two spatial dimensions (2D) (or on faces in three spatial dimensions) and a staggered electric field on cell corners (or on edges in three spatial dimensions) so that the computed magnetic field preserves discrete divergence-free. To achieve this, a weighted flux interpolation approach based on [5, 23, 31] is introduced in this paper to compute the z-component of the electric field. While multidimensional Riemann solvers are the best way to achieve multidimensional upwinding for the electric field, our present unstructured mesh code does not have the requisite infrastructure for supporting multidimensional Riemann solvers [11–13, 35]. In a subsequent paper, we will report on the incorporation of multidimensional Riemann solvers with globally divergence-free methods for MHD on unstructured meshes.

To achieve high-order accuracy, a new divergence-free WENO reconstruction method is developed to reconstruct a cell centered magnetic field from the staggered collocation of magnetic fields on cell edges in two spatial dimensions. Our proposed reconstruction method makes sure that the reconstructed approximations to the magnetic field represented by piecewise smooth polynomials supported on triangular cells match exactly at cell edges in the following sense: for magnetic field approximations supported on two triangles sharing a common cell edge, the component of the magnetic field in the direction of the edge unit normal is uniquely defined even at higher order. Namely, on the cell edge, the normal component of the reconstructed magnetic field is C^0 continuous. For the cell centered variables, the WENO reconstruction described in [21, 26] is utilized. Numerical experiments show that the present divergence-free WENO reconstruction-based finite volume scheme is robust and accurate.

The paper is organized as follows. Section 2 describes the CT type finite volume formulation to solve the ideal MHD equations. We start by introducing governing equations, notations for domain partition and discretization. Specifically, the proposed weighted flux interpolation approach to compute the z-component of the electric field is explained in Subsection 2.3. Section 3 presents the proposed reconstruction algorithm. The second-order accurate and the third-order accurate divergence-free WENO reconstruction methods are catalogued in detail in Subsection 3.1. Numerical tests are given in Section 4 to demonstrate the accuracy and non-oscillatory properties of the proposed scheme by computing smooth solution and shock wave related problems. We draw conclusions in Section 5.

2 Finite volume formulation

Ideal MHD governing equations in the conservation form can be expressed as

$$\partial_t \mathbf{U} + \partial_x \mathbf{F}(\mathbf{U}) + \partial_y \mathbf{G}(\mathbf{U}) = 0, \tag{2.1}$$

where

$$\mathbf{U} = \left(\rho, \rho u_x, \rho u_y, \rho u_z, \varepsilon, B_x, B_y, B_z\right)^T, \tag{2.2}$$

https://doi.org/10.4208/cicp.050814.040915a Published online by Cambridge University Press

and

$$\mathbf{F}(\mathbf{U})=\begin{pmatrix}\rho u_x\\ \rho u_x^2+p-B_x^2\\ \rho u_x u_y-B_xB_y\\ \rho u_x u_z-B_xB_z\\ (\varepsilon+p)u_x-B_x(\mathbf{u}\cdot\mathbf{B})\\ 0\\ (u_xB_y-u_yB_x)\\ -(u_zB_x-u_xB_z)\end{pmatrix},\quad \mathbf{G}(\mathbf{U})=\begin{pmatrix}\rho u_y\\ \rho u_x u_y-B_xB_y\\ \rho u_y^2+p-B_y^2\\ \rho u_y u_z-B_yB_z\\ (\varepsilon+p)u_y-B_y(\mathbf{u}\cdot\mathbf{B})\\ -(u_xB_y-u_yB_x)\\ 0\\ (u_yB_z-u_zB_y)\end{pmatrix}. \tag{2.3}$$

Here $p=p_{gas}+\mathbf{B}\cdot\mathbf{B}/2$ is the total pressure, p_{gas} is the gas pressure that satisfies the following equation of state

$$p_{gas}=(\gamma-1)\Big(\varepsilon-\frac{1}{2}\rho\mathbf{u}\cdot\mathbf{u}-\frac{1}{2}\mathbf{B}\cdot\mathbf{B}\Big),$$

with $\mathbf{u}=(u_x,u_y,u_z)^T$ and $\mathbf{B}=(B_x,B_y,B_z)^T$. For a 2D ideal MHD problem, we have

$$E_z=-u_xB_y+u_yB_x. \tag{2.4}$$

We employ the CT approach and the Godunov type finite volume scheme to solve Eq. (2.1). To this end, the physical domain $\Omega\subset\mathbb{R}^2$ is partitioned into a collection of $\mathcal{N}$ triangular cells $\mathcal{K}_i$ so that $\Omega=\bigcup_{i=1}^{\mathcal{N}}\mathcal{K}_i$ and we define the partition

$$\mathcal{T}_h=\{\mathcal{K}_i:i=1,\cdots,\mathcal{N}\}. \tag{2.5}$$

For simplicity, we assume that there are no hanging nodes in the partition $\mathcal{T}_h$. We collect cell edges $\mathcal{L}_j$ to form

$$\mathfrak{E}_h=\{\mathcal{L}_j:j=1,\cdots,\mathcal{N}_{\mathfrak{E}}\}, \tag{2.6}$$

where $\mathcal{N}_{\mathfrak{E}}$ is the total number of edges in the partition. For every cell edge $\mathcal{L}_j$, we uniquely identify an edge unit normal $\mathbf{n}_j=(n_{x,j},n_{y,j})$ and tangent $\boldsymbol{\zeta}_j$. Here $\boldsymbol{\zeta}_j$ is obtained by rotating $\mathbf{n}_j$ 90 degrees in the counterclockwise direction. Following $\boldsymbol{\zeta}_j$ direction, the start point of $\mathcal{L}_j$ is $\mathbf{x}_{j,s}=(x_{j,s},y_{j,s})$, and the end point of $\mathcal{L}_j$ is $\mathbf{x}_{j,e}=(x_{j,e},y_{j,e})$. For convenience in discussion, we also use the notation $\partial\mathcal{K}_{i,l}$, $l=1,2,3$ to denote edges of cell $\mathcal{K}_i$, and we define a mapping between the local cell edge index l of cell $\mathcal{K}_i$ and the global edge index j:

$$l=\ell_i(j)\quad\text{and}\quad j=\ell_i^{-1}(l)\quad\text{for } l=1,2,3, \tag{2.7}$$

such that $\partial\mathcal{K}_{i,l}=\mathcal{L}_{\ell_i^{-1}(l)}$. The mesh parameter h is defined to be

$$\begin{aligned}h_{\mathcal{K}_i}&=\text{ the diameter of }\mathcal{K}_{\mathrm{i}}=\text{ the longest side of }\mathcal{K}_{\mathrm{i}},\\ h&=\max_{\mathcal{K}_i\in\mathcal{T}_h}h_{\mathcal{K}_i}.\end{aligned} \tag{2.8}$$

https://doi.org/10.4208/cicp.050814.040915a Published online by Cambridge University Press

Lastly, we collect vertices $\mathcal{V}_J$ of cells in $\mathcal{T}_h$ to form

$$\mathfrak{V}_h=\{\mathcal{V}_J:J=1,\cdots,\mathcal{N}_{\mathfrak{V}}\}, \tag{2.9}$$

where $\mathcal{N}_{\mathfrak{V}}$ is the total number of vertices in $\mathcal{T}_h$.

Following the CT formulation, we place normal component of the magnetic field in the edge unit normal direction at the cell edges; the z-component of the electric field E_z at the cell vertices; and the conservative variables ρ, $\rho\mathbf{u}$, ε and B_z on the cells. The magnetic field is always initialized to be divergence-free. This is done by using a vector potential approach, see [7] for details. The Godunov type finite volume scheme is utilized to evolve ρ,$\rho\mathbf{u}$, ε and B_z on the cells and the normal component of the magnetic field within the xy-plane on the cell edges. To evaluate E_z at cell vertices, the flux-interpolated approach introduced by Balsara and Spicer [5] is further developed here.

For convenience in discussion, we introduce notations $\mathbf{U}^H=(\rho,\rho\mathbf{u},\varepsilon,B_z)^T$ and $\mathbf{B}^{xy}=(B_x,B_y)^T$ so that

$$\partial_t\mathbf{U}^H+\partial_x\mathbf{F}^H(\mathbf{U})+\partial_y\mathbf{G}^H(\mathbf{U})=0, \tag{2.10}$$

where

$$\mathbf{F}^H(\mathbf{U})=\begin{pmatrix}\rho u_x\\ \rho u_x^2+p-B_x^2\\ \rho u_xu_y-B_xB_y\\ \rho u_xu_z-B_xB_z\\ (\varepsilon+p)u_x-B_x(\mathbf{u}\cdot\mathbf{B})\\ -(u_zB_x-u_xB_z)\end{pmatrix},\quad \mathbf{G}^H(\mathbf{U})=\begin{pmatrix}\rho u_y\\ \rho u_xu_y-B_xB_y\\ \rho u_y^2+p-B_y^2\\ \rho u_yu_z-B_yB_z\\ (\varepsilon+p)u_y-B_y(\mathbf{u}\cdot\mathbf{B})\\ u_yB_z-u_zB_y\end{pmatrix}. \tag{2.11}$$

And

$$\partial_t\mathbf{B}^{xy}+\partial_x\mathbf{F}^B(\mathbf{U})+\partial_y\mathbf{G}^B(\mathbf{U})=0, \tag{2.12}$$

where

$$\mathbf{F}^B(\mathbf{U})=\begin{pmatrix}0\\ u_xB_y-u_yB_x\end{pmatrix},\quad \mathbf{G}^B(\mathbf{U})=\begin{pmatrix}-u_xB_y+u_yB_x\\ 0\end{pmatrix}. \tag{2.13}$$

Thus solving Eq. (2.1) is equivalent to solving Eqs. (2.10) and (2.12) together.

2.1 Semi-discrete finite volume scheme for the cell-centered $\mathbf{U}^H$

Taking the cell $\mathcal{K}_i$, $i=1,\cdots,\mathcal{N}$, in partition $\mathcal{T}_h$ as a discrete control volume, we formulate the semi-discrete finite volume method for solving Eq. (2.10) by integrating (2.10) over the cell $\mathcal{K}_i$

$$\frac{d}{dt}\overline{\mathbf{U}}^H_{k,i}(t)+\frac{1}{|\mathcal{K}_i|}\sum_{l=1}^{3}\int_{\partial\mathcal{K}_{i,l}}(\mathbf{F}^H_k,\mathbf{G}^H_k)\cdot\boldsymbol{n}_{\mathcal{K}_{i,l}}d\Gamma=0, \tag{2.14}$$

where $\overline{\mathbf{U}}^H_{k,i}(t)$ is the cell average of the kth ($k=1,\cdots,6$) component of $\mathbf{U}^H$ on $\mathcal{K}_i$, $\mathbf{F}^H_k$ is the kth component of $\mathbf{F}^H$, $\mathbf{G}^H_k$ is the kth component of $\mathbf{G}^H$, and $\boldsymbol{n}_{\mathcal{K}_{i,l}}$ is the outward unit

https://doi.org/10.4208/cicp.050814.040915a Published online by Cambridge University Press

normal of the edge $\partial\mathcal{K}_{i,l}$ of the cell $\mathcal{K}_i$. On edge $\partial\mathcal{K}_{i,l}$, the cell outward unit normal $\boldsymbol{n}_{\mathcal{K}_{i,l}}$ is either $\boldsymbol{n}_{\mathcal{K}_{i,l}}=\mathbf{n}_{\ell_i^{-1}(l)}$ or $\boldsymbol{n}_{\mathcal{K}_{i,l}}=-\mathbf{n}_{\ell_i^{-1}(l)}$. $|\mathcal{K}_i|$ is a shorthand notation for the area of $\mathcal{K}_i$.

To solve Eq. (2.14) numerically, we evaluate the flux integral by Gaussian quadrature rule with the exact value of $(\mathbf{F}^H,\mathbf{G}^H)\cdot\boldsymbol{n}_{\mathcal{K}_{i,l}}$ being replaced by the Lax-Friedrichs flux $\mathbf{F}^*(x,y,t)$ given by

$$\mathbf{F}_k^*(x,y,t)=\frac{1}{2}\left[(\mathbf{F}_k^H(\mathbf{U}^-),\mathbf{G}_k^H(\mathbf{U}^-))+(\mathbf{F}_k^H(\mathbf{U}^+),\mathbf{G}_k^H(\mathbf{U}^+))\right]\cdot\boldsymbol{n}_{\mathcal{K}_{i,l}}-\frac{\alpha}{2}(\mathbf{U}_k^{H,+}-\mathbf{U}_k^{H,-}). \quad (2.15)$$

Here α is taken as an estimate of the largest absolute value of eigenvalues of the Jacobian $(\partial/\partial\mathbf{U})\left((\mathbf{F},\mathbf{G})\cdot\boldsymbol{n}_{\mathcal{K}_{i,l}}\right)$; $\mathbf{U}^-$ (or $\mathbf{U}^{H,-}$) and $\mathbf{U}^+$ (or $\mathbf{U}^{H,+}$) are the numerical values of $\mathbf{U}$ (or $\mathbf{U}^H$) inside the triangle and outside the triangle at the Gaussian point. To this end, we obtain the following semi-discrete finite volume scheme for solving Eq. (2.10)

$$\frac{d}{dt}\overline{\mathbf{U}}_{h,k,i}^H(t)+\frac{1}{|\mathcal{K}_i|}\sum_{l=1}^{3}\int_{\partial\mathcal{K}_{i,l}}\mathbf{F}_k^*d\Gamma=0, \quad (2.16)$$

where $\overline{\mathbf{U}}_{h,k,i}^H(t)$ is the approximate cell average of the kth component of $\mathbf{U}^H$ on the cell $\mathcal{K}_i$.

2.2 Semi-discrete finite volume scheme for the edge-centered normal component of $\mathbf{B}^{xy}$

The 2D constrained transport finite volume scheme developed in the present paper evolves cell edge-length-averaged magnetic field located on the edges of grid cells. Specifically on every cell edge $\mathcal{L}_j\in\mathfrak{E}_h$, we solve Eq. (2.12) to evolve the normal component of $\mathbf{B}^{xy}$ with respect to the defined cell edge unit normal $\mathbf{n}_j$. Denote the normal and tangential contribution of $\mathbf{B}^{xy}$ in directions given by $\mathbf{n}_j$ and $\boldsymbol{\zeta}_j$ to be B_n and B_ζ respectively. We rewrite Eq. (2.12) by B_n and B_ζ to obtain

$$\partial_t\begin{pmatrix}B_n\\B_\zeta\end{pmatrix}+\partial_n\begin{pmatrix}0\\u_nB_\zeta-u_\zeta B_n\end{pmatrix}+\partial_\zeta\begin{pmatrix}-u_nB_\zeta+u_\zeta B_n\\0\end{pmatrix}=0. \quad (2.17)$$

Here u_n and u_ζ are the components of velocity $\mathbf{u}$ in the $\mathbf{n}_j$ and $\boldsymbol{\zeta}_j$ directions respectively.

Let $\overline{B_{n,j}}$ be the edge-length-averaged B_n on the edge $\mathcal{L}_j$ defined by

$$\overline{B_{n,j}}=\frac{1}{|\mathcal{L}_j|}\int_{\mathcal{L}_j}B_nd\zeta, \quad (2.18)$$

where $|\mathcal{L}_j|$ is a shorthand notation for the length of the edge $\mathcal{L}_j$. Integrating Eq. (2.17) over the cell edge $\mathcal{L}_j$, the semi-discrete finite volume scheme to evolve $\overline{B_{n,j}}$ numerically on $\mathcal{L}_j$ is expressed as

$$\frac{d}{dt}\overline{B_{h,n,j}}=-\frac{E_z(\mathbf{x}_{j,e})-E_z(\mathbf{x}_{j,s})}{|\mathcal{L}_j|}, \quad (2.19)$$

https://doi.org/10.4208/cicp.050814.040915a Published online by Cambridge University Press

since

$$E_z = -u_n B_\zeta + u_\zeta B_n.$$

Here $\overline{B_{h,n,j}}$ is the approximate cell edge-length-averaged B_n on $\mathcal{L}_j$. $E_z(\mathbf{x}_{j,e})$ is numerical approximation of the z-component of $\mathbf{E}$ at the end point $\mathbf{x}_{j,e}$ of $\mathcal{L}_j$, and $E_z(\mathbf{x}_{j,s})$ is numerical approximation of the z-component of $\mathbf{E}$ at the start point $\mathbf{x}_{j,s}$ of $\mathcal{L}_j$. The method to compute E_z is described in Section 2.3.

2.3 Flux interpolation method to compute E_z at the vertices of the mesh

In our scheme, one has to obtain the electric field E_z at vertices of the triangular mesh in order to solve Eq. (2.19). See Fig. 1. In [5], it was shown that there is a dualism between the electric field and the properly upwinded flux. In fluid dynamics, such a flux takes on contributions that are upwinded normal to a zone face. For MHD, the electric field at the vertex $\mathcal{V}$ in Fig. 1 should take on properly upwinded contributions from all possible directions. This necessarily would require a multi-dimensional Riemann solver. For rectangular meshes, such a multi-dimensional Riemann solver has been presented in [11]. Unfortunately, a multi-dimensional Riemann solver that works for MHD on triangular meshes has only been presented very recently in the literature [12] and our present code does not have the infrastructure for accommodating such a Riemann solver. For that reason, we use the available ideas on multi-dimensional upwinding from [5], and the idea of doubling dissipation in each direction from [23,31].

Below we describe an algorithm to compute the z-component of the electrical field E_z at each vertices of the mesh. The algorithm results in an upwinded choice of E_z in a multi-dimensional fashion.

See Fig. 1. Let's assume triangles $\mathcal{K}_0,\cdots,\mathcal{K}_4$ meet at the vertex $\mathcal{V}=(x_\mathcal{V},y_\mathcal{V})$. The edges shared by triangles are labeled by $\mathcal{L}_0,\cdots,\mathcal{L}_4$ and the associated unit normals of edges by $\mathbf{n}_0,\cdots,\mathbf{n}_4$ respectively.

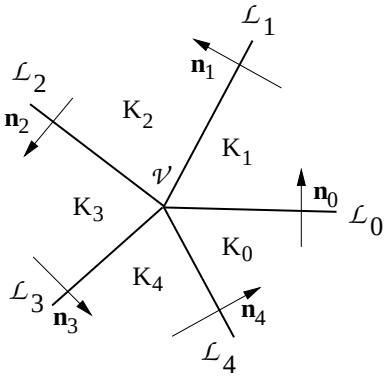


Figure 1: The stencil to compute E_z at the vertex $\mathcal{V}$. Cell edges $\mathcal{L}_0,\cdots,\mathcal{L}_4$ which separate triangular cells $\mathcal{K}_0,\cdots,\mathcal{K}_4$ all have one end at $\mathcal{V}$. $\mathbf{n}_0,\cdots,\mathbf{n}_4$ are unit normals of these edges respectively.

https://doi.org/10.4208/cicp.050814.040915a Published online by Cambridge University Press

On each edge $\mathcal{L}_l$, $l=0,\cdots,4$, using Eq. (2.4), which shows the dualism between E_z and flux, we obtain

$$E_{z,l}(x_{\mathcal{V}},y_{\mathcal{V}})=-\mathbf{F}_{LF,6}\left(\mathbf{U}^-(x_{\mathcal{V}},y_{\mathcal{V}}),\mathbf{U}^+(x_{\mathcal{V}},y_{\mathcal{V}})\right), \tag{2.20}$$

from numerical flux interpolation. Here $(x_{\mathcal{V}},y_{\mathcal{V}})$ are the coordinates of $\mathcal{V}$. $\mathbf{F}_{LF}$ is the Lax-Friedrichs flux for solving Eq. (2.1); and $\mathbf{F}_{LF,6}$ is the 6th component of $\mathbf{F}_{LF}$. Let $\mathcal{K}_l^{\text{int}}$ denote the interior of cell $\mathcal{K}_l$.

$$\begin{aligned}&\mathbf{U}^-(x_{\mathcal{V}},y_{\mathcal{V}})=\lim_{(x,y)\to(x_{\mathcal{V}},y_{\mathcal{V}})}\mathbf{U}(x,y,t), \quad \text{where } (x,y)\in\mathcal{K}_l^{\text{int}},\\ &\mathbf{U}^+(x_{\mathcal{V}},y_{\mathcal{V}})=\lim_{(x,y)\to(x_{\mathcal{V}},y_{\mathcal{V}})}\mathbf{U}(x,y,t), \quad \text{where } (x,y)\in\mathcal{K}_{(l+1)\bmod(n_v+1)}^{\text{int}}.\end{aligned}$$

Here $(l+1)\bmod(n_v+1)$ is the modulus operation. Thus

$$\mathbf{F}_{LF}(\mathbf{U}^-,\mathbf{U}^+)=\frac{1}{2}\left[\left(\mathbf{F}(\mathbf{U}^-),\mathbf{G}(\mathbf{U}^-)\right)+\left(\mathbf{F}(\mathbf{U}^+),\mathbf{G}(\mathbf{U}^+)\right)\right]\cdot\mathbf{n}_l-\alpha(\mathbf{U}^+-\mathbf{U}^-). \tag{2.21}$$

Here α is taken as an upper bound for the eigenvalues of the Jacobian in the normal direction $\mathbf{n}_l$ of edge $\mathcal{L}_l$.

If the flow is locally smooth, we can take the arithmetic average

$$E_z(x_{\mathcal{V}},y_{\mathcal{V}})=\frac{1}{1+n_v}\sum_{l=0}^{n_v}E_{z,l}(x_{\mathcal{V}},y_{\mathcal{V}}) \tag{2.22}$$

to obtain a unique E_z at the vertex $\mathcal{V}$. Here n_v is the total number of edges meeting at the common vertex minus 1 and $n_v=4$ for the case shown in Fig. 1.

However,when discontinuities are present it is beneficial to allow the evaluation of E_z to locally adjust to those discontinuities. To achieve this, we design switches to detect strong magnetosonic shocks and strongly compressive motions and the direction of propagation of the discontinuity. For this purpose, we first use a least squares approach to construct linear profiles of pressure and velocity at the vertex $\mathcal{V}=(x_{\mathcal{V}},y_{\mathcal{V}})$ respectively as follows.

Let each of the components of $\hat{\mathbf{v}}(x,y)=\left(p_{gas}(x,y),u_x(x,y),u_y(x,y)\right)^T$ be represented by a linear polynomial

$$\hat{v}_s(x,y)=\overline{v}_s+\frac{\triangle_x v_s}{h}(x-x_{\mathcal{V}})+\frac{\triangle_y v_s}{h}(y-y_{\mathcal{V}}). \tag{2.23}$$

Here $\hat{v}_s(x,y)$, $s=1,2,3$, is the sth component of $\hat{\mathbf{v}}(x,y)$. h is the mesh parameter. $(\triangle_x v_s,\triangle_y v_s)$ is the undivided difference approximation to the gradient of the exact profile of pressure or velocity at $\mathcal{V}$.

We compute on $\mathcal{K}_l$, $l=0,\cdots,4$, pressure $p_{gas,l}$ and velocity $(u_{x,l},u_{y,l})$ from cell average values of $\mathbf{U}$ at the cell centers. Let $\{\mathbf{v}_l=(p_{gas,l},u_{x,l},u_{y,l})^T:\ l=0,\cdots,4\}$ be the collection of these values.

https://doi.org/10.4208/cicp.050814.040915a Published online by Cambridge University Press

Parameter values $\overline{v}_s$, $\triangle_x v_s$ and $\triangle_y v_s$ of Eq. (2.23) are then determined by solving

$$\left\{\overline{v}_s+\frac{\triangle_x v_s}{h}(x_l-x_{\mathcal{V}})+\frac{\triangle_y v_s}{h}(y_l-y_{\mathcal{V}})=v_{s,l},\quad l=0,\cdots,4,\right.$$

in the least square sense. Here (x_l,y_l) are the coordinates of the cell center of $\mathcal{K}_l$; $v_{s,l}$ stands for the value of the sth component of $\mathbf{v}_l$ on cell $\mathcal{K}_l$, which are $p_{gas,l}$, $u_{x,l}$ and $u_{y,l}$ respectively.

Based on linear least squares fitted pressure and velocity profiles described by Eq. (2.23) at the vertex $\mathcal{V}$, we are ready to define switches.

The first switch, **SW1**, which is used to pick out strong magnetosonic shocks or configuration that may develop into such a shock, is accomplished by taking the undivided gradient of the pressure $\left(\triangle_x p_{gas},\triangle_y p_{gas}\right)^T$ at the vertex $\mathcal{V}$ and comparing it with the minimum pressure in the vicinity. **SW1** is switched on if

$$|\triangle_x p_{gas}|+|\triangle_y p_{gas}|>\beta\min(p_{gas,0},\cdots,p_{gas,n_v}) \tag{2.24}$$

and is switched off otherwise. We use $\beta=0.5$. Values of $\triangle_x p_{gas}$ and $\triangle_y p_{gas}$ are taken from Eq. (2.23) for pressure.

The second switch, **SW2**, which is used to pick out strong compressive motions at the vicinity of the vertex $\mathcal{V}$, is accomplished by comparing the undivided divergence of the velocity to the smallest local signal speed. **SW2** is switched on if

$$-\delta\min(C_0,\cdots,C_{n_v})>(\triangle_x u_x+\triangle_y u_y) \tag{2.25}$$

and is switched off otherwise. We use $\delta=0.1$. Values of $\triangle_x u_x$ and $\triangle_y u_y$ are taken from Eq. (2.23) for velocity. On cell $\mathcal{K}_l$,

$$C_l=\left(\frac{\gamma p_{gas,l}}{\overline{\rho}_l}+\frac{\overline{\mathbf{B}}_l\cdot\overline{\mathbf{B}}_l}{\overline{\rho}_l}\right)^{1/2},\quad l=0,\cdots,n_v,$$

where $\overline{\rho}_l$ and $\overline{\mathbf{B}}_l=\left(\overline{B_{xl}},\overline{B_{yl}},\overline{B_{zl}}\right)^T$ are average values of density and magnetic field on $\mathcal{K}_l$.

When either **SW1** or **SW2** is switched on, it means that the region has a shock or large variation in motion in it. In this case, we need to pick out the direction along which we want to upwind the evaluation of the electric field. We use a weighted combination described below to do that.

We estimate the direction $\mathbf{n}_{\mathrm{S}}=(n_{\mathrm{S},x},n_{\mathrm{S},y})^T$ of the strong shock in the vicinity of the vertex $\mathcal{V}$ by

$$n_{\mathrm{S},x}=\frac{\triangle_x p_{gas}}{\sqrt{(\triangle_x p_{gas})^2+(\triangle_y p_{gas})^2}}, \tag{2.26}$$

$$n_{\mathrm{S},y}=\frac{\triangle_y p_{gas}}{\sqrt{(\triangle_x p_{gas})^2+(\triangle_y p_{gas})^2}}. \tag{2.27}$$

https://doi.org/10.4208/cicp.050814.040915a Published online by Cambridge University Press

Then for each $E_{z,l}$ computed by Eq. (2.20), we compute the associated weight w_l by

$$w_l = \frac{\alpha_l}{\sum_{s=0}^{n_v} \alpha_s}, \tag{2.28}$$

where α_l is defined by

$$\alpha_l = (\mathbf{n}_S \cdot \mathbf{n}_l)^4 + 10^{-6}. \tag{2.29}$$

Here the small number 10^{-6} is to avoid division by zero in Eq. (2.28), and the power 4 is chosen based on numerical experiments.

To this end, we compute $E_z(x_\mathcal{V}, y_\mathcal{V})$ by

$$E_z(x_\mathcal{V}, y_\mathcal{V}) = \sum_{l=0}^{n_v} w_l E_{z,l}(x_\mathcal{V}, y_\mathcal{V}) \tag{2.30}$$

at vertex $\mathcal{V}$ when discontinuity or strong compression is present. If neither **SW1** nor **SW2** is switched on, then we say that the flow is locally smooth. In this case, we use Eq. (2.22) to evaluate $E_z(x_\mathcal{V}, y_\mathcal{V})$.

Image a situation where four cartesian zones come together at a vertex. Also say that the flow is mesh-aligned in the x-direction. Then Eq. (2.30) will pick out the electric field from the two x-flux directions and both will be properly upwinded. Admittedly, some transverse contribution will be missed. On unstructured mesh, this fully multidimensional contribution can only be picked up by a multidimensional Riemann solver, see [46]. Such a Riemann solver was not available to us when this work was done, however, we endorse the use of such a multidimensional Riemann solver.

To summarize, the following steps are taken to evolve the normal components of the magnetic field B_n supported on cell edges:

Step a. For each vertex of the mesh $\mathcal{V}_j$: $j=1,\cdots,\mathcal{N}_\mathfrak{V}$, we identify all cell edges that meet at $\mathcal{V}_j$ and apply the flux interpolation method described in Subsection 2.3 to compute E_z at the vertex. Specifically, E_z is computed by either Eq. (2.22) or Eq. (2.30) depending on whether switch **SW1** or **SW2** is switched on.

Step b. We then solve Eq. (2.19) by a TVD Runge-Kutta time discretization method [39] to evolve cell edge-length-averaged $\overline{B_{n,j}}$ numerically on each cell edge.

It is worth noting that for the CT type formulation to solve ideal MHD equations, the normal components B_n in the direction of cell edge unit normal of the magnetic field have to satisfy the following consistency condition

$$0 = \oint_{\partial\mathcal{K}_i} B_n d\zeta, \tag{2.31}$$

in order to evolve the magnetic field in a divergence-free manner. Here $\mathcal{K}_i$ is a grid cell, $\partial\mathcal{K}_i$ is its cell boundary and $\partial\mathcal{K}_i \equiv \partial\mathcal{K}_{i,1} \bigcup \partial\mathcal{K}_{i,2} \bigcup \partial\mathcal{K}_{i,3}$. Notice that $B_n = \mathbf{B} \cdot \boldsymbol{n}_{\mathcal{K}_i}$, and $\boldsymbol{n}_{\mathcal{K}_i}$

https://doi.org/10.4208/cicp.050814.040915a Published online by Cambridge University Press

is the cell edge unit normal pointing outwards from the cell. Eq. (2.31) is obtained by integrating $\nabla\cdot\mathbf{B}=0$ over cell $\mathcal{K}_i$ and applying the divergence theorem.

Next we show that our CT formulation satisfies the consistency condition given by Eq. (2.31) thanks to our flux interpolation method to compute the z-component E_z of the electric field at each vertex $\mathcal{V}_j$ of the mesh $\mathcal{T}_h$.

To see this, let's assume that unit normals of edges $\partial\mathcal{K}_{i,l}$, $l=1,2,3$ of $\mathcal{K}_i$ point outwards so that the end point of edge $\partial\mathcal{K}_{i,l}$ is the start point of edge $\partial\mathcal{K}_{i,(l+1)\text{mod}(3)}$ for $l=1,2,3$.

Eq. (2.19) implies

$$\frac{d\left(|\partial\mathcal{K}_{i,l}|\overline{B_{h,n,\ell_i^{-1}(l)}}\right)}{dt}=E_z(\mathbf{x}_{i,l,e})-E_z(\mathbf{x}_{i,l,s}),\quad l=1,2,3, \tag{2.32}$$

where $\mathbf{x}_{i,l,e}$ and $\mathbf{x}_{i,l,s}$ represent the end point and start point of edge $\partial\mathcal{K}_{i,l}$ respectively. ℓ_i^{-1} is the mapping between the local cell edge index l of cell $\mathcal{K}_i$ and the global edge index j defined in Eq. (2.7). Since values of E_z at each vertex of the mesh are uniquely computed by the flux interpolation method, by adding Eq. (2.32) defined on edges of $\mathcal{K}_i$ together we obtain

$$\sum_{l=1}^{3}\frac{d\left(|\partial\mathcal{K}_{i,l}|\overline{B_{h,n,\ell_i^{-1}(l)}}\right)}{dt}=0.$$

Therefore our computed normal components $\overline{B_{h,n,j}}$ on cell edges satisfies the following discrete analogues of the consistency condition (2.31):

$$|\partial\mathcal{K}_{i,1}|\overline{B_{h,n,\ell_i^{-1}(1)}}+|\partial\mathcal{K}_{i,2}|\overline{B_{h,n,\ell_i^{-1}(2)}}+|\partial\mathcal{K}_{i,3}|\overline{B_{h,n,\ell_i^{-1}(3)}}=0 \tag{2.33}$$

on edges $\partial\mathcal{K}_{i,l}$ of cell $\mathcal{K}_i$, provided the magnetic field is divergence-free initially. In [7], we have shown that the above equation is satisfied as long as the same electric field at vertices is used for updating the face centered magnetic field. In other words, this is a Yee type scheme on unstructured meshes.

2.4 Time discretization

The method of lines approach is used to evolve the solution on the triangulated domain. Specifically, the third-order accurate TVD Runge-Kutta method [39] is used to solve ordinary differential equations (2.16) and (2.19).

3 WENO-based reconstruction

The main ingredient of a high-order accurate finite volume scheme is a reconstruction algorithm, which reconstructs a smooth and high degree polynomial approximation of the solution from average values computed by the base finite volume scheme at the end of every Runge-Kutta stage. In return, the reconstructed polynomial is used for evaluating

https://doi.org/10.4208/cicp.050814.040915a Published online by Cambridge University Press

numerical fluxes in the subsequent calculation. In this section, we solve the following two sub-problems of reconstruction:

Sub-problem 1. Given edge-length-averaged normal component $\overline{B_{n,j}}$ of $\mathbf{B}^{xy}$ defined on cell edges $\mathcal{L}_j \in \mathfrak{E}_h$ and a positive integer q, for each cell $\mathcal{K}_i$, reconstruct an essentially non-oscillatory and divergence-free magnetic field $\widetilde{\widetilde{\mathbf{B}}}_i^{xy}$ supported on $\mathcal{K}_i$. Here $\widetilde{\widetilde{\mathbf{B}}}_i^{xy} \in P_q(\mathcal{K}_i)^2$. $P_q(\mathcal{K}_i)$ is the space of polynomials of degree at most q supported on $\mathcal{K}_i$. $\widetilde{\widetilde{\mathbf{B}}}_i^{xy}$ is a $(q+1)$th-order accurate approximation to exact $\mathbf{B}^{xy}$ (when it is smooth) on cell $\mathcal{K}_i$. $\widetilde{\widetilde{\mathbf{B}}}_i^{xy}$ has the following three properties: 1) $\widetilde{\widetilde{\mathbf{B}}}_i^{xy}$ is divergence-free. 2) $\widetilde{\widetilde{\mathbf{B}}}_i^{xy}$ is conservative on the edge, namely,

$$\frac{1}{|\partial\mathcal{K}_{i,l}|}\int_{\partial\mathcal{K}_{i,l}} \widetilde{\widetilde{\mathbf{B}}}_i^{xy}\cdot\mathbf{n}_{\ell_i^{-1}(l)}d\zeta = \overline{B_{n,\ell_i^{-1}(l)}}, \quad l=1,2,3. \tag{3.1}$$

Here $\partial\mathcal{K}_{i,l}$ is the lth edge of cell $\mathcal{K}_i$; $\mathbf{n}_{\ell_i^{-1}(l)}$ is the associated unit normal of this edge; $|\partial\mathcal{K}_{i,l}|$ is its length. $\overline{B_{n,\ell_i^{-1}(l)}}$ is the edge-length-averaged normal component of the magnetic field on $\partial\mathcal{K}_{i,l}$. 3) If $\widetilde{\widetilde{\mathbf{B}}}_i^{xy}$ and $\widetilde{\widetilde{\mathbf{B}}}_{i'}^{xy}$ are supported on two grid cells $\mathcal{K}_i$ and $\mathcal{K}_{i'}$ sharing a common edge with unit normal $\hat{\mathbf{n}}$, the normal components of $\widetilde{\widetilde{\mathbf{B}}}_i^{xy}$ and $\widetilde{\widetilde{\mathbf{B}}}_{i'}^{xy}$ in $\hat{\mathbf{n}}$ direction agree precisely on this edge.

For our proposed scheme, we present a reconstruction algorithm in Section 3.1 to solve this sub-problem at the end of each Runge-Kutta stage by using mean values $\overline{B_{h,n,j}}$, which are numerical approximation to $\overline{B_{n,j}}$.

Sub-problem 2. Given cell average values $\overline{v}_i$ of a function $v(x,y)$ on each cell $\mathcal{K}_i$ and a positive integer q, for each cell $\mathcal{K}_i$, reconstruct an essentially non-oscillatory polynomial $\widetilde{P}_i(x,y)$ of degree at most q which has the mean value $\overline{v}_i$ and is a $(q+1)$th-order accurate approximation to $v(x,y)$ on $\mathcal{K}_i$ (when $v(x,y)$ is smooth). For our ideal MHD problem, at the end of every Runge-Kutta stage, this problem is solved for $\overline{v}_i$ replaced by the cell average values of the every component of $\mathbf{U}^H$ computed by the base finite volume scheme.

Before we describe the algorithm to solve these two reconstruction problems, we first recall several relevant concepts which will be used later in this section. The level-0 von Neumann neighborhood of a triangle $\mathcal{K}\in\mathcal{T}_h$ contains the edge adjacent neighbors of $\mathcal{K}$ and is defined to be the set

$$\mathfrak{N}^0(\mathcal{K}) = \left\{\widetilde{\mathcal{K}}\in\mathcal{T}_h\setminus\{\mathcal{K}\} : \widetilde{\mathcal{K}}\cap\mathcal{K} \text{ is an edge of } \mathcal{K}\right\}.$$

Here we neglect the subscript "i" of cells for convenience. The level-r von Neumann neighborhood is defined by the recursive definition

$$\mathfrak{N}^r(\mathcal{K}) = \left(\bigcup_{\widetilde{\mathcal{K}}\in\mathfrak{N}^{r-1}(\mathcal{K})} \mathfrak{N}^{r-1}(\widetilde{\mathcal{K}})\right)\setminus\{\mathcal{K}\}, \quad \text{for } r\geq 1.$$

https://doi.org/10.4208/cicp.050814.040915a Published online by Cambridge University Press

For instance, the level-1 von Neumann neighborhood of $\mathcal{K}$ is obtained by merging level-0 von Neumann neighborhoods of cells in $\mathfrak{N}^0(\mathcal{K})$ which are edge adjacent neighbors of $\mathcal{K}$. This level-r von Neumann neighborhood concept was introduced in [26].

A critical component for the success of reconstruction on triangular meshes is the selection of a set of admissible stencils. Generally, this set should contain isotropic (or centered) stencil for achieving good approximation in smooth regions, and anisotropic (or one-sided and reverse-sided) stencils to avoid interpolation across discontinuities [21, 26].

In order to construct these anisotropic stencils, the sector search algorithm [24, 26] is utilized to construct forward sectors as well as backward sectors. Fig. 2(b) shows three forward sectors $FS_s, s=1,2,3$ of cell $\mathcal{K}_0$. A forward sector is spanned by a pair of edges of $\mathcal{K}_0$. Fig. 2(c) shows three backward sectors $BS_s, s=1,2,3$ of $\mathcal{K}_0$. A backward sector is defined by having its origin at the midpoint of an edge of $\mathcal{K}_0$ and its two boundary edges passing through the other two midpoints of remaining edges of $\mathcal{K}_0$.

When we perform a WENO reconstruction for a cell $\mathcal{K}\in\mathcal{T}_h$, in addition to construct a central stencil, within each of the sectors of $\mathcal{K}$, we construct either an one-sided stencil (when it is a forward sector) or a reverse-sided stencil (when it is a backward sector). Additionally, when we construct an anisotropic stencil, we only include cells in von Neumann neighbors of $\mathcal{K}$, whose barycenters lie in the corresponding forward or backward sector.

3.1 Summary of divergence-free WENO-based reconstruction algorithm for $\mathbf{B}^{xy}$ on cell

In this subsection we summarize a new divergence-free WENO-based reconstruction strategy for reconstructing the magnetic field on triangular grids based on our recent work [14] and [7, 9]. This solves the ***Sub-problem 1***. The reconstructed $\widetilde{\widetilde{\mathbf{B}}}_i^{xy}$ supported on cell $\mathcal{K}_i$ is: 1) divergence-free on $\mathcal{K}_i$ internally, 2) a $(q+1)$th-order accurate approximation to exact $\mathbf{B}^{xy}$ on $\mathcal{K}_i$, and 3) uniquely defined on edges of $\mathcal{K}_i$. It conserves the facially averaged magnetic field component on each face of $\mathcal{K}_i$.

Moreover, suppose two cells $\mathcal{K}_i, \mathcal{K}_{i'}\in\mathcal{T}_h$ share an edge $\mathcal{L}_j$, namely $\mathcal{K}_i\bigcap\mathcal{K}_{i'}=\mathcal{L}_j$, and let $\widetilde{\widetilde{\mathbf{B}}}_i^{xy}(x,y)$ and $\widetilde{\widetilde{\mathbf{B}}}_{i'}^{xy}(x,y)$ be reconstructed magnetic field approximations on these two cells respectively. $\widetilde{\widetilde{\mathbf{B}}}_i^{xy}(x,y)$ and $\widetilde{\widetilde{\mathbf{B}}}_{i'}^{xy}(x,y)$ satisfy

$$\widetilde{\widetilde{\mathbf{B}}}_i^{xy}(x,y)\cdot\mathbf{n}_j=\widetilde{\widetilde{\mathbf{B}}}_{i'}^{xy}(x,y)\cdot\mathbf{n}_j \qquad \text{for } (x,y)\in\mathcal{L}_j. \tag{3.2}$$

Eq. (3.2) implies that the normal component of the reconstructed magnetic field is C^0 continuous on the grid cell edges.

We summarize the ***algorithm for reconstructing magnetic field*** as follows:

Step 1. For every grid cell $\mathcal{K}_i$, we identify a set of admissible reconstruction stencils $\mathfrak{T}_B=\{T_B^{(m)}: m=1,\cdots,7\}$ using the method introduced in [21, 24, 26]. Here $T_B^{(1)}$ represents

https://doi.org/10.4208/cicp.050814.040915a Published online by Cambridge University Press

the central stencil; $T_B^{(2)}$, $T_B^{(3)}$ and $T_B^{(4)}$ are the one-sided stencils constructed in each of the forward sectors of $\mathcal{K}_i$ respectively; and $T_B^{(5)}$, $T_B^{(6)}$ and $T_B^{(7)}$ are the reverse-sided stencils constructed in each of the backward sectors of $\mathcal{K}_i$ respectively. This choice of stencils allows to better limit oscillations of polynomial approximation of the solution supported on $\mathcal{K}_i$.

Step 2. For each stencil, we use cell edge-length-averaged values of normal component $\overline{B_{h,n,j}}$ defined on edges of cells contained in the stencil to reconstruct preliminarily a divergence-free magnetic field $\mathbf{B}_i^{xy,(m)}$, $m=1,\cdots,7$, with every component of $\mathbf{B}_i^{xy,(m)}$ represented by a up to qth degree polynomial function.

Step 3. For each preliminarily reconstructed $\mathbf{B}_i^{xy,(m)}$, a smoothness indicator ω_m is computed with $\sum_{m=1}^{7}\omega_m=1$. The nonlinearly stabilized WENO reconstruction $\widetilde{\mathbf{B}}_i^{xy}$ is defined by a weighted combination $\sum_{m=1}^{7}\omega_m\mathbf{B}_i^{xy,(m)}$ and is exactly divergence-free.

Step 4. On each cell edge $\mathcal{L}_j$, $j=1,\cdots,\mathcal{N}_{\mathfrak{E}}$, we reconstruct a polynomial approximation $\widetilde{B}_{n,j}$ to the edge-centered normal component of the magnetic field in the direction of edge unit normal with $(q+1)$th-order accuracy. We use the reconstructed $\widetilde{\mathbf{B}}_i^{xy}$ supported on cells in *Step 3* to accomplish this task.

Step 5. Denote the cell edges of the grid cell $\mathcal{K}_i$ by $\partial\mathcal{K}_{i,l}$, $l=1,2,3$, and relabel the reconstructed $\widetilde{B}_{n,j}$ on these edges by $\widetilde{B}_{n,\ell_i^{-1}(l)}$ respectively. For each grid cell $\mathcal{K}_i$, we use $\widetilde{B}_{n,\ell_i^{-1}(l)}$, $l=1,2,3$ (and $\overline{B_{h,n,j}}$ from edge adjacent cells of $\mathcal{K}_i$ if needed) to reconstruct a divergence-free magnetic field $\widetilde{\widetilde{\mathbf{B}}}_i^{xy}$ on $\mathcal{K}_i$.

For the conciseness of the paper, we provide details for implementing the second-order in Subsection 3.2. Readers can find details of implementing the third-order case in Appendix A.

3.2 Second-order accurate reconstruction for $\mathbf{B}^{xy}$

To explain the ***algorithm for reconstructing magnetic field*** clearly, we first describe the second-order accurate reconstruction case. We note that the preliminarily reconstructed $\mathbf{B}^{xy,(m)}$, WENO combined $\widetilde{\mathbf{B}}^{xy}$ and reconstructed $\widetilde{\widetilde{\mathbf{B}}}^{xy}$ all belong to $\{\mathbf{v}\in P_1(\mathcal{K}_i)^2:\nabla\cdot\mathbf{v}=0\}$. $\mathbf{B}^{xy,(m)}=\left(B_x^{(m)},B_y^{(m)}\right)^T$ is represented as:

$$\begin{aligned} B_x^{(m)}(x,y)&=a_{0,m}+a_{1,m}x+a_{2,m}y,\\ B_y^{(m)}(x,y)&=b_{0,m}+b_{1,m}x+b_{2,m}y. \end{aligned} \tag{3.3}$$

Here we drop the subscript "i" for convenience.

https://doi.org/10.4208/cicp.050814.040915a Published online by Cambridge University Press

The divergence-free condition $\nabla\cdot\mathbf{B}^{xy,(m)}=0$ gives the equation

$$a_{1,m}+b_{2,m}=0, \tag{3.4}$$

for linear polynomial representation of $\mathbf{B}^{xy}$ by matching coefficients. This reduces one of the degrees of freedom in reconstructing $\mathbf{B}^{xy,(m)}$.

Fig. 2 shows stencils used to reconstruct $\widetilde{\widetilde{\mathbf{B}}}_0^{xy}$ on cell $\mathcal{K}_0$. The central stencil is shown

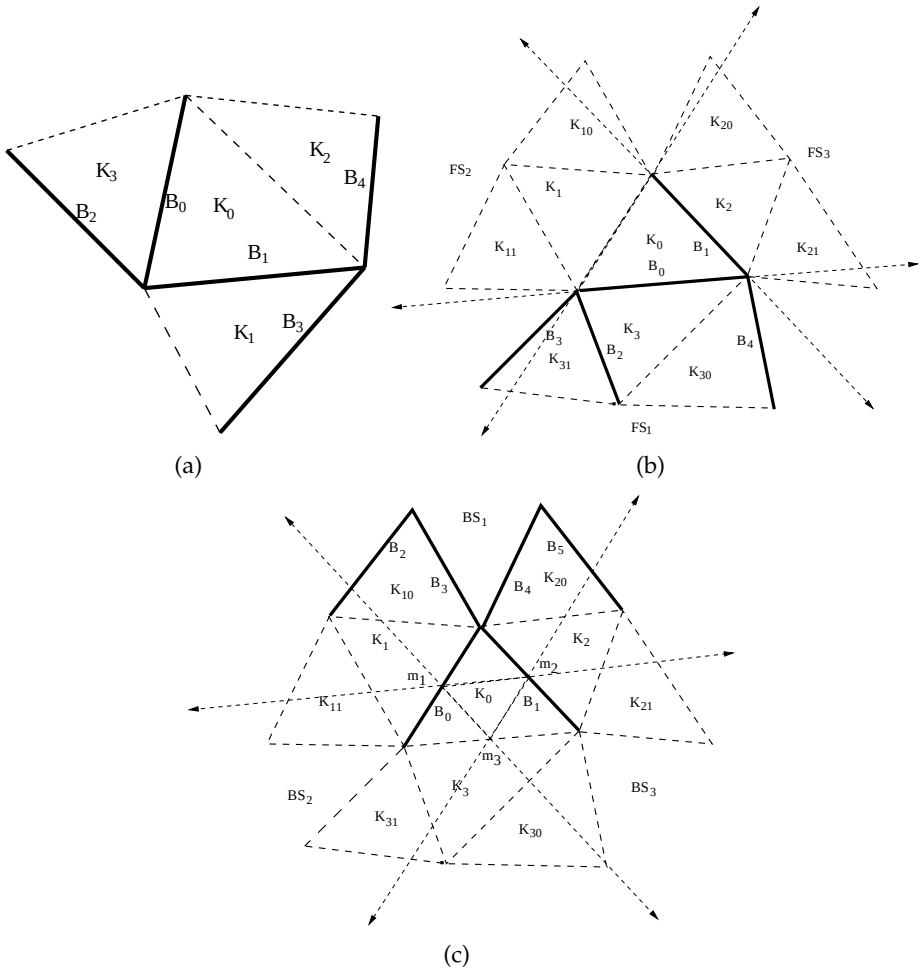


Figure 2: Stencils for reconstructing second order accurate cell-centered divergence-free magnetic field on cell $\mathcal{K}_0$. Normal components of the magnetic field on solid line edges are utilized. (a) The central stencil. (b) Three forward sectors FS_1, FS_2 and FS_3 of cell $\mathcal{K}_0$ formed by spanning a pair of edges of $\mathcal{K}_0$ respectively. The cells of three one-sided stencils formed in each of the forward sector are shown here. (c) Three backward sectors BS_1, BS_2 and BS_3 of $\mathcal{K}_0$. A backward sector is defined by having its origin at the midpoint of an edge of $\mathcal{K}_0$ and its two boundary edges passing through the other two midpoints of remaining edges. The cells of three reverse-sided stencils formed in each of the backward sector are shown here. Note that the same notations are used for different normal components of the magnetic field and cells in (a), (b) and (c) to avoid introducing too many notations.

https://doi.org/10.4208/cicp.050814.040915a Published online by Cambridge University Press

in Fig. 2(a). Fig. 2(b) shows three forward sectors FS_s,$s=1,2,3$ of $\mathcal{K}_0$ as well as cells used to construct corresponding one-sided stencils. Fig. 2(c) shows three backward sectors BS_s,$s=1,2,3$ of $\mathcal{K}_0$ and cells chosen to construct corresponding reverse-sided stencils. The details of constructing one-sided and reverse-sided stencils in these sectors and reconstructing linear polynomial $\widetilde{\widetilde{\mathbf{B}}}_0^{xy}$ supported on $\mathcal{K}_0$ are given below.

3.2.1 Preliminary second-order accurate reconstruction on central stencil

See Fig. 2(a). The central stencil consists of $\mathcal{K}_0$, and its three adjacent neighbors $\mathcal{K}_s$,$s=1,2,3$, which are in the level-0 von Neumann neighbor of $\mathcal{K}_0$.

On $\mathcal{K}_0$, we arbitrarily choose two cell edge-length-averaged values of normal components of $\mathbf{B}^{xy}$, denoted by B_0 and B_1. On each of $\mathcal{K}_s$, $s=1,2,3$, we choose one cell edge-length-averaged value of normal components of $\mathbf{B}^{xy}$ defined on the cell edge which is not the common edge between $\mathcal{K}_0$ and $\mathcal{K}_s$, and denote these average values by B_2, B_3 and B_4 respectively. The cell edges on which these values are defined are relabeled by $\mathcal{L}_s:s=0,\cdots,4$ for convenience. The solid lines in Fig. 2(a) indicate these edges. We then solve

$$\begin{cases} a_{1,m}+b_{2,m}=0, \\ \dfrac{1}{|\mathcal{L}_s|}\displaystyle\int_{\mathcal{L}_s}\mathbf{B}^{xy,(m)}\cdot\mathbf{n}_s d\zeta=B_s, \quad s=0,\cdots,4, \end{cases} \tag{3.5}$$

to obtain a candidate $\mathbf{B}^{xy,(1)}$. Here $m=1$; $|\mathcal{L}_s|$ is the length of $\mathcal{L}_s$; and $\mathbf{n}_s$ is the unit normal of $\mathcal{L}_s$.

Notice that our choice of cell edges is such that we never form closed loops of edges. This is because the divergence-free condition ensures that each closed loop has one redundant piece of information which can be computed by Eq. (2.33). Also notice that Eq. (3.3) only has five independent degrees of freedom and we have selected five edges which do not close from the central stencil. We remark that this general principle also applies to reconstructing $\mathbf{B}^{xy}$ on other stencils.

Finally we point out that for this central stencil, there are other possible ways to choose cell edges for reconstruction. See Fig. 2(a). For instance, we could use values defined on the dashed line edges from every neighboring cells of $\mathcal{K}_0$ together with ones defined on the solid line edges of $\mathcal{K}_0$ to reconstruct the polynomial. This is also the case for reconstruction by using other stencils. However, we notice that as long as we follow the principle of choosing edges close to $\mathcal{K}_0$, the results are not sensitive to choices of edges.

3.2.2 Preliminary second-order accurate reconstruction on one-sided stencils

Fig. 2(b) shows forward sectors and corresponding one-sided stencils utilized for reconstruction. In Fig. 2(b), cells $\mathcal{K}_1$, $\mathcal{K}_2$ and $\mathcal{K}_3$ are three neighbors of $\mathcal{K}_0$; and $\mathcal{K}_{s0}$, $\mathcal{K}_{s1}$ are two neighbors of $\mathcal{K}_s$ (other than $\mathcal{K}_0$), $s=1,2,3$. We form three one-sided stencils: $T_B^{(2)}=$

https://doi.org/10.4208/cicp.050814.040915a Published online by Cambridge University Press

$\{\mathcal{K}_0,\mathcal{K}_3,\mathcal{K}_{30},\mathcal{K}_{31}\}$ in FS_1; $T_B^{(3)}=\{\mathcal{K}_0,\mathcal{K}_1,\mathcal{K}_{10},\mathcal{K}_{11}\}$ in FS_2; and $T_B^{(4)}=\{\mathcal{K}_0,\mathcal{K}_2,\mathcal{K}_{20},\mathcal{K}_{21}\}$ in FS_3.

With every one-sided stencil $T_B^{(m)}$, $m=2,3,4$, we will utilize cell edge-length-averaged values of normal component of the magnetic field $\mathbf{B}^{xy}$ on cell edges to reconstruct preliminarily a divergence-free polynomial in the form of (3.3). Take stencil $T_B^{(2)}$ for example. On $\mathcal{K}_0$, we utilize two average values of normal component of $\mathbf{B}^{xy}$ defined on its two edges respectively, and denote them by B_0 and B_1. On $\mathcal{K}_3$, we use one average value of normal component of $\mathbf{B}^{xy}$ defined on the cell edge which is not the common edge between $\mathcal{K}_0$ and $\mathcal{K}_3$, and denote it by B_2. On each of $\mathcal{K}_{30}$ and $\mathcal{K}_{31}$, one average value defined on the cell edge which is not shared by $\mathcal{K}_3$ and $\mathcal{K}_{30}$ (or by $\mathcal{K}_3$ and $\mathcal{K}_{31}$) is employed respectively, and denote them by B_3 and B_4.

We now use $\{B_s:s=0,\cdots,4\}$ to reconstruct preliminarily a piecewise linear $\widetilde{\mathbf{B}}^{xy,(2)}$ by solving Eq. (3.5). We similarly compute on the other two one-sided stencils to obtain two candidates respectively, denoted by $\mathbf{B}^{xy,(3)}$, and $\mathbf{B}^{xy,(4)}$.

3.2.3 Preliminary second-order accurate reconstruction on reverse-sided stencils

The reverse-sided stencils are constructed by using cells within the backward sectors. Fig. 2(c) shows reverse-sided stencils which are constructed in the backward sector BS_s, $s=1,2,3$ for reconstructing $\mathbf{B}^{xy}$ on $\mathcal{K}_0$. Here cells $\mathcal{K}_1$, $\mathcal{K}_2$ and $\mathcal{K}_3$ are three neighbors of $\mathcal{K}_0$; and $\mathcal{K}_{s0}$, $\mathcal{K}_{s1}$ are two neighbors of $\mathcal{K}_s$ (other than $\mathcal{K}_0$), $s=1,2,3$. We construct three reverse-sided stencils: $T_B^{(5)}=\{\mathcal{K}_0,\mathcal{K}_{10},\mathcal{K}_{20}\}$ in BS_1; $T_B^{(6)}=\{\mathcal{K}_0,\mathcal{K}_{11},\mathcal{K}_{31}\}$ in BS_2; and $T_B^{(7)}=\{\mathcal{K}_0,\mathcal{K}_{21},\mathcal{K}_{30}\}$ in BS_3.

Unlike the central or one-sided stencil case, here we employ a constrained least square method to solve the reconstruction problem by using each of the reverse-sided stencils. Due to the divergence-free condition, in principle, we only need 5 additional conditions to uniquely determine functions (3.3). However, a reverse-sided stencil can provide 6 admissible average values of normal component of $\mathbf{B}^{xy}$ (or 6 conditions to determine (3.3)). See Fig. 2(c). Take the stencil $T_B^{(5)}$ for example. The edges on which the defined average values are employed for preliminary reconstruction are indicated by solid lines. On $\mathcal{K}_0$, we can use two edge values B_0 and B_1. On $\mathcal{K}_{10}$, we can use B_2 and B_3; and on $\mathcal{K}_{20}$, we have B_4 and B_5 to use. To avoid a bias in choosing values from $T_B^{(5)}$, we use all of these 6 average values and solve the following system of linear equations with linear constraints for the preliminary reconstruction:

$$\begin{cases} \dfrac{1}{|\mathcal{L}_s|}\displaystyle\int_{\mathcal{L}_s}\mathbf{B}^{xy,(m)}\cdot\mathbf{n}_s d\zeta=B_s, & s=2,\cdots,5, \end{cases} \tag{3.6}$$

subject to:

$$\begin{cases} a_{1,m}+b_{2,m}=0, \\ \dfrac{1}{|\mathcal{L}_{s'}|}\displaystyle\int_{\mathcal{L}_{s'}}\mathbf{B}^{xy,(m)}\cdot\mathbf{n}_{s'} d\zeta=B_{s'}, & s'=0,1. \end{cases} \tag{3.7}$$

https://doi.org/10.4208/cicp.050814.040915a Published online by Cambridge University Press

When solving this constrained least square problem, Eq. (3.7) is satisfied exactly; while Eq. (3.6) is satisfied in the least square sense. To improve the divergence-free aspect of the solution to this constrained least square problem on stencil cells other than $\mathcal{K}_0$, one can substitute Eq. (3.4) into Eq. (3.6) before solving (3.6)-(3.7). This ensures that the preliminarily reconstructed magnetic field on the cell of interest, $\mathcal{K}_0$, is divergence-free, and matches the magnetic field defined on the cell edges bounding $\mathcal{K}_0$ by mean values exactly. Additionally, the preliminarily reconstructed magnetic field is the best approximation to the magnetic field on other cells in the reverse-sided stencil.

We denote candidates obtained by solving Eqs. (3.6)-(3.7)- in a constrained least square manner for every reverse-sided stencils $\mathbf{B}^{xy,(5)}$, $\mathbf{B}^{xy,(6)}$ and $\mathbf{B}^{xy,(7)}$ respectively.

3.2.4 Computation of weights for second-order accurate WENO reconstruction

We now apply a weighted combination of $\{\mathbf{B}^{xy,(m)}: m=1,\cdots,7\}$ to finalize $\widetilde{\mathbf{B}}_0^{xy}$ using the idea of WENO [22, 40]. This accomplishes *Step 3* of the ***algorithm for reconstructing magnetic field***. We note that this step is for obtaining the non-oscillatory property for the reconstructed magnetic field, yet not to increase the accuracy from that of $\{\mathbf{B}^{xy,(m)}: m=1,\cdots,7\}$ to that of $\widetilde{\mathbf{B}}_0^{xy}$, as the original WENO method does [25, 40].

For each $\mathbf{B}^{xy,(m)}$ represented by Eq. (3.3), we compute a quantity α_m, which is the reciprocal of a smoothness measure by

$$\alpha_m=\frac{b_m}{\epsilon+(a_{1,m})^2+(a_{2,m})^2+(b_{1,m})^2+(b_{2,m})^2},\qquad m=1,\cdots,7.$$

Here we take $\epsilon=10^{-6}$ to avoid division by zero. $b_m=10$ when $m=1$; and $b_m=1$ otherwise. This follows the idea in [27]. The parameter b_m allows to have more weight on the central stencil, which provides better accuracy when the solution is smooth.

The weight ω_m is computed by

$$\omega_m=\frac{\alpha_m}{\sum_{l=1}^{7}\alpha_l}.$$

Finally, we reconstruct the piecewise linear polynomial approximation $\widetilde{\mathbf{B}}_0^{xy}$ on $\mathcal{K}_0$ by

$$\widetilde{\mathbf{B}}_0^{xy}=\sum_{m=1}^{7}\omega_m\mathbf{B}^{xy,(m)}.$$

Notice that $\widetilde{\mathbf{B}}_0^{xy}$ satisfies the divergence-free condition: $\nabla\cdot\widetilde{\mathbf{B}}_0^{xy}=0$ exactly. Moreover, it is easy to verify that

$$\frac{1}{|\partial\mathcal{K}_{0,l}|}\int_{\partial\mathcal{K}_{0,l}}\widetilde{\mathbf{B}}_0^{xy}\cdot\mathbf{n}_{0,l}d\zeta=\overline{B_{n,\ell_0^{-1}(l)}},\quad l=1,2,3. \tag{3.8}$$

This completes *Step 3* of the ***algorithm for reconstructing magnetic field*** for the second-order accurate case.

https://doi.org/10.4208/cicp.050814.040915a Published online by Cambridge University Press

3.2.5 Second-order accurate reconstruction for $\widetilde{B}_{n,j}$ on cell edges

After reconstructing non-oscillatory $\widetilde{\mathbf{B}}_i^{xy}$, $i=1,\cdots,\mathcal{N}$ on each cells, we now reconstruct a linear and non-oscillatory polynomial approximation to the normal components of the magnetic field $\widetilde{B}_{n,j}$ supported on cell edges for each $\mathcal{L}_j$, $j=1,\cdots,\mathcal{N}_{\mathfrak{E}}$.

Assume that the edge $\mathcal{L}_j$ is not on the boundary of the domain Ω and has edge unit normal $\mathbf{n}_j$. Let's denote two grid cells sharing $\mathcal{L}_j$ by $\mathcal{K}_{\mathcal{L}_i}$ and $\mathcal{K}_{\mathcal{L}_{i'}}$ and the reconstructed magnetic field on each of them from *Step 3* by $\widetilde{\mathbf{B}}_i^{xy}$ and $\widetilde{\mathbf{B}}_{i'}^{xy}$ respectively.

We parameterize edge $\mathcal{L}_j$ by function $\mathbf{r}(\zeta)=(x(\zeta),y(\zeta))$ with

$$\mathbf{r}(\zeta)=\mathbf{x}_{j,m}+\triangle\mathbf{x}_j\zeta,\quad -1\le\zeta\le 1. \tag{3.9}$$

Here $\mathbf{x}_{j,m}=\frac{\mathbf{x}_{j,e}+\mathbf{x}_{j,s}}{2}$ and $\triangle\mathbf{x}_j=\frac{\mathbf{x}_{j,e}-\mathbf{x}_{j,s}}{2}$. $\mathbf{x}_{j,s}=(x_{j,s},y_{j,s})$ and $\mathbf{x}_{j,e}=(x_{j,e},y_{j,e})$ are the start and end points of $\mathcal{L}_j$ respectively.

The normal component of $\widetilde{\mathbf{B}}_i^{xy}$ in $\mathbf{n}_j$ direction and defined on $\mathbf{r}(\zeta)$ is therefore

$$\begin{aligned}B_{n,i}(\zeta)&=\mathbf{n}_j\cdot\widetilde{\mathbf{B}}_i^{xy}(x(\zeta),y(\zeta))\\&=\left(n_{x,j}\left(\widetilde{a}_{0,i}+\widetilde{a}_{1,i}x_{j,m}+\widetilde{a}_{2,i}y_{j,m}\right)+n_{y,j}\left(\widetilde{b}_{0,i}+\widetilde{b}_{1,i}x_{j,m}+\widetilde{b}_{2,i}y_{j,m}\right)\right)\\&\quad+\left(n_{x,j}\left(\widetilde{a}_{1,i}\triangle x_j+\widetilde{a}_{2,i}\triangle y_j\right)+n_{y,j}\left(\widetilde{b}_{1,i}\triangle x_j+\widetilde{b}_{2,i}\triangle y_j\right)\right)\zeta,\end{aligned} \tag{3.10}$$

which is a linear polynomial with respect to parameter ζ. Similarly the normal component of $\widetilde{\mathbf{B}}_{i'}^{xy}$ along $\mathbf{r}(\zeta)$ is

$$\begin{aligned}B_{n,i'}(\zeta)&=\mathbf{n}_j\cdot\widetilde{\mathbf{B}}_{i'}^{xy}(x(\zeta),y(\zeta))\\&=\left(n_{x,j}\left(\widetilde{a}_{0,i'}+\widetilde{a}_{1,i'}x_{j,m}+\widetilde{a}_{2,i'}y_{j,m}\right)+n_{y,j}\left(\widetilde{b}_{0,i'}+\widetilde{b}_{1,i'}x_{j,m}+\widetilde{b}_{2,i'}y_{j,m}\right)\right)\\&\quad+\left(n_{x,j}\left(\widetilde{a}_{1,i'}\triangle x_j+\widetilde{a}_{2,i'}\triangle y_j\right)+n_{y,j}\left(\widetilde{b}_{1,i'}\triangle x_j+\widetilde{b}_{2,i'}\triangle y_j\right)\right)\zeta.\end{aligned} \tag{3.11}$$

For convenience in discussion let's rewrite $B_{n,i}(\zeta)$ and $B_{n,i'}(\zeta)$ in the following forms:

$$\begin{aligned}&B_{n,i}(\zeta)=\hat{a}_j+\hat{b}_i\zeta,\\&B_{n,i'}(\zeta)=\hat{a}_j+\hat{b}_{i'}\zeta,\qquad -1\le\zeta\le 1,\end{aligned} \tag{3.12}$$

with

$$\begin{aligned}\hat{a}_j&\equiv\left(n_{x,j}\left(\widetilde{a}_{0,i}+\widetilde{a}_{1,i}x_{j,m}+\widetilde{a}_{2,i}y_{j,m}\right)+n_{y,j}\left(\widetilde{b}_{0,i}+\widetilde{b}_{1,i}x_{j,m}+\widetilde{b}_{2,i}y_{j,m}\right)\right)\\&=\left(n_{x,j}\left(\widetilde{a}_{0,i'}+\widetilde{a}_{1,i'}x_{j,m}+\widetilde{a}_{2,i'}y_{j,m}\right)+n_{y,j}\left(\widetilde{b}_{0,i'}+\widetilde{b}_{1,i'}x_{j,m}+\widetilde{b}_{2,i'}y_{j,m}\right)\right),\\\hat{b}_i&\equiv\left(n_{x,j}\left(\widetilde{a}_{1,i}\triangle x_j+\widetilde{a}_{2,i}\triangle y_j\right)+n_{y,j}\left(\widetilde{b}_{1,i}\triangle x_j+\widetilde{b}_{2,i}\triangle y_j\right)\right),\\\hat{b}_{i'}&\equiv\left(n_{x,j}\left(\widetilde{a}_{1,i'}\triangle x_j+\widetilde{a}_{2,i'}\triangle y_j\right)+n_{y,j}\left(\widetilde{b}_{1,i'}\triangle x_j+\widetilde{b}_{2,i'}\triangle y_j\right)\right).\end{aligned}$$

https://doi.org/10.4208/cicp.050814.040915a Published online by Cambridge University Press

Notice that $B_{n,i}(\zeta)$ and $B_{n,i'}(\zeta)$ must have the same constant coefficient $\hat{a}_j$, which is equal to $\overline{B_{n,j}}$, and in general $\hat{b}_i \neq \hat{b}_{i'}$. This is due to conservative nature of the reconstruction which conserves edge-length averaged values of the normal components of the magnetic field on cell edges when reconstructing $\widetilde{\mathbf{B}}_i^{xy}$ and $\widetilde{\mathbf{B}}_{i'}^{xy}$. See also Eq. (3.8). Finally, we determine the reconstructed $\widetilde{B}_{n,j}$ supported on $\mathcal{L}_j$ by

$$\widetilde{B}_{n,j}(\zeta) = \hat{a}_j + \hat{b}_j \zeta, \quad -1 \leq \zeta \leq 1, \tag{3.13}$$

where $\hat{b}_j = \text{minmod}(\hat{b}_i, \hat{b}_{i'})$ and the minmod function is defined by

$$\text{minmod}(c_1,c_2) = \begin{cases} c_1 & \text{if } |c_1| < |c_2| \text{ and } c_1 c_2 > 0, \\ c_2 & \text{if } |c_2| < |c_1| \text{ and } c_1 c_2 > 0, \\ 0 & \text{otherwise.} \end{cases} \tag{3.14}$$

3.2.6 Second-order accurate non-oscillatory, divergence-free reconstruction for $\widetilde{\widetilde{\mathbf{B}}}_i^{xy}$ with continuous normal component

Step 5 of the ***algorithm for reconstructing magnetic field*** is to reconstruct a divergence-free $\widetilde{\widetilde{\mathbf{B}}}_i^{xy}(x,y)$ on each cell $\mathcal{K}_i$ using reconstructed $\widetilde{B}_{n,\ell_i^{-1}(l)}$, $l=1,2,3$ given by Eq. (3.13) on edges of $\mathcal{K}_i$. This is achieved by letting $\widetilde{\widetilde{\mathbf{B}}}_i^{xy}(x,y)$ match $\widetilde{B}_{n,\ell_i^{-1}(l)}$, $l=1,2,3$ exactly along each edge $\mathcal{L}_{\ell_i^{-1}(l)}$ respectively and satisfy the divergence-free condition. The details to do this are given below.

Let $\widetilde{\widetilde{\mathbf{B}}}_i^{xy} = (\widetilde{\widetilde{B}}_x, \widetilde{\widetilde{B}}_y)^T$ be represented by

$$\begin{aligned} \widetilde{\widetilde{B}}_x(x,y) &= \widetilde{\widetilde{a}}_0 + \widetilde{\widetilde{a}}_1 x + \widetilde{\widetilde{a}}_2 y, \\ \widetilde{\widetilde{B}}_y(x,y) &= \widetilde{\widetilde{b}}_0 + \widetilde{\widetilde{b}}_1 x + \widetilde{\widetilde{b}}_2 y. \end{aligned} \tag{3.15}$$

On each edge $\mathcal{L}_{\ell_i^{-1}(l)}$ of $\mathcal{K}_i$, we represent the normal component $B_{n,\ell_i^{-1}(l)}(\zeta)$ of $\widetilde{\widetilde{\mathbf{B}}}_i^{xy}(x,y)$ by

$$\begin{aligned} & B_{n,\ell_i^{-1}(l)}(\zeta) = \mathbf{n}_{\ell_i^{-1}(l)} \cdot \widetilde{\widetilde{\mathbf{B}}}_i^{xy}(x(\zeta),y(\zeta)) \\ &= \left(n_{x,\ell_i^{-1}(l)} \left(\widetilde{\widetilde{a}}_0 + \widetilde{\widetilde{a}}_1 x_{\ell_i^{-1}(l),m} + \widetilde{\widetilde{a}}_2 y_{\ell_i^{-1}(l),m} \right) + n_{y,\ell_i^{-1}(l)} \left(\widetilde{\widetilde{b}}_0 + \widetilde{\widetilde{b}}_1 x_{\ell_i^{-1}(l),m} + \widetilde{\widetilde{b}}_2 y_{\ell_i^{-1}(l),m} \right) \right) \\ &\quad + \left(n_{x,\ell_i^{-1}(l)} \left(\widetilde{\widetilde{a}}_1 \triangle x_{\ell_i^{-1}(l)} + \widetilde{\widetilde{a}}_2 \triangle y_{\ell_i^{-1}(l)} \right) + n_{y,\ell_i^{-1}(l)} \left(\widetilde{\widetilde{b}}_1 \triangle x_{\ell_i^{-1}(l)} + \widetilde{\widetilde{b}}_2 \triangle y_{\ell_i^{-1}(l)} \right) \right) \zeta, \end{aligned} \tag{3.16}$$

where the parametric equation $\mathbf{r}(\zeta) = (x(\zeta), y(\zeta))$ of the edge is defined by Eq. (3.9).

We then solve the following system of linear equations for $\widetilde{\widetilde{a}}_0, \widetilde{\widetilde{a}}_1, \widetilde{\widetilde{a}}_2, \widetilde{\widetilde{b}}_0, \widetilde{\widetilde{b}}_1$, and $\widetilde{\widetilde{b}}_2$ to

https://doi.org/10.4208/cicp.050814.040915a Published online by Cambridge University Press

reconstruct $\widetilde{\widetilde{\mathbf{B}}}_i^{xy}(x,y)$ supported on $\mathcal{K}_i$

$$\begin{cases} \text{E1: } \widetilde{\widetilde{a}}_1+\widetilde{\widetilde{b}}_2=0, \\ \text{E2: } n_{x,\ell_i^{-1}(l)}\left(\widetilde{\widetilde{a}}_1\triangle x_{\ell_i^{-1}(l)}+\widetilde{\widetilde{a}}_2\triangle y_{\ell_i^{-1}(l)}\right)+n_{y,\ell_i^{-1}(l)}\left(\widetilde{\widetilde{b}}_1\triangle x_{\ell_i^{-1}(l)}+\widetilde{\widetilde{b}}_2\triangle y_{\ell_i^{-1}(l)}\right) \\ \quad =\hat{b}_{\ell_i^{-1}(l)} \qquad \text{for } l=1,2,3, \\ \text{E3: } n_{x,\ell_i^{-1}(l')}\left(\widetilde{\widetilde{a}}_0+\widetilde{\widetilde{a}}_1 x_{\ell_i^{-1}(l'),m}+\widetilde{\widetilde{a}}_2 y_{\ell_i^{-1}(l'),m}\right)+n_{y,\ell_i^{-1}(l')}\left(\widetilde{\widetilde{b}}_0+\widetilde{\widetilde{b}}_1 x_{\ell_i^{-1}(l'),m}+\widetilde{\widetilde{b}}_2 y_{\ell_i^{-1}(l'),m}\right) \\ \quad =\hat{a}_{\ell_i^{-1}(l')} \qquad \text{for } l'=1,2. \end{cases} \tag{3.17}$$

We note that Eq. (3.17.E1) is for $\widetilde{\widetilde{\mathbf{B}}}_i^{xy}(x,y)$ to satisfy the divergence-free condition. The set of linear equations (3.17.E2) is for $\widetilde{\widetilde{\mathbf{B}}}_i^{xy}(x,y)$ matching with linear moments of $B_{n,\ell_i^{-1}(l)}$ on edge $\mathcal{L}_{\ell_i^{-1}(l)}$ respectively; while the set of linear equations (3.17.E3) is to match with the zeroth moments of $B_{n,\ell_i^{-1}(l)}$ on $\mathcal{L}_{\ell_i^{-1}(l)}$ respectively. Notice that Eq. (3.17.E3) only consists of two equations, which makes it look like that the edge-length-averaged values of $\widetilde{\widetilde{\mathbf{B}}}_i^{xy}(x,y)$ on edges will only agree with two edge-length-averaged values of $\widetilde{B}_{n,\ell_i^{-1}(l')}$, $l'=1,2$. However, by $\nabla\cdot\widetilde{\widetilde{\mathbf{B}}}_i^{xy}(x,y)=0$, we have

$$\sum_{l=1}^{3}\frac{1}{|\mathcal{L}_{\ell_i^{-1}(l)}|}\int_{\mathcal{L}_{\ell_i^{-1}(l)}}\widetilde{\widetilde{\mathbf{B}}}_i^{xy}\cdot\boldsymbol{n}_{\mathcal{K}_{i,l}}d\zeta=0, \tag{3.18}$$

where $\boldsymbol{n}_{\mathcal{K}_{i,l}}$ is the lth edge unit normal pointing outwards from the cell $\mathcal{K}_i$. By Eq. (3.17.E3), we have either

$$\begin{cases} \dfrac{1}{|\mathcal{L}_{\ell_i^{-1}(l')}|}\displaystyle\int_{\mathcal{L}_{\ell_i^{-1}(l')}}\widetilde{\widetilde{\mathbf{B}}}_i^{xy}\cdot\boldsymbol{n}_{\mathcal{K}_{i,l'}}d\zeta=\overline{B_{h,n,\ell_i^{-1}(l')}}\,, & \text{if } \boldsymbol{n}_{\mathcal{K}_{i,l'}}=\mathbf{n}_{\ell_i^{-1}(l')},\ l'=1,2, \\ \text{or} & \\ \dfrac{1}{|\mathcal{L}_{\ell_i^{-1}(l')}|}\displaystyle\int_{\mathcal{L}_{\ell_i^{-1}(l')}}\widetilde{\widetilde{\mathbf{B}}}_i^{xy}\cdot\boldsymbol{n}_{\mathcal{K}_{i,l'}}d\zeta=-\overline{B_{h,n,\ell_i^{-1}(l')}}\,, & \text{if } \boldsymbol{n}_{\mathcal{K}_{i,l'}}=-\mathbf{n}_{\ell_i^{-1}(l')},\ l'=1,2. \end{cases} \tag{3.19}$$

Eqs. (3.18) and (3.19) imply that

$$\frac{1}{|\mathcal{L}_{\ell_i^{-1}(3)}|}\int_{\mathcal{L}_{\ell_i^{-1}(3)}}\widetilde{\widetilde{\mathbf{B}}}_i^{xy}\cdot\mathbf{n}_{\ell_i^{-1}(3)}d\zeta=\overline{B_{h,n,\ell_i^{-1}(3)}}\,.$$

Thus we have shown that the reconstructed $\widetilde{\widetilde{\mathbf{B}}}_i^{xy}$ also satisfies the consistency condition (2.33).

Moreover, by Eqs. (3.17.E2) and (3.17.E3), the reconstructed second-order accurate $\{\widetilde{\widetilde{\mathbf{B}}}_i^{xy}(x,y):\ i=1,\cdots\mathcal{N}\}$ satisfies Eq. (3.2), namely, the normal component of the reconstructed magnetic field in edge normal direction is $\mathcal{C}^0$ continuous on cell edges.

https://doi.org/10.4208/cicp.050814.040915a Published online by Cambridge University Press

This finishes reconstructing a second-order accurate, divergence-free magnetic field with continuous normal components. For the numerical scheme formulated in this paper, this reconstruction is applied at the end of the every Runge-Kutta stage for the second-order accurate case. In the next subsection, we explain how to reconstruct a third-order accurate, non-oscillatory and divergence-free magnetic field with continuous normal component.

3.3 WENO finite volume reconstruction for $\mathbf{U}^H$

In this section we describe an algorithm to reconstruct polynomials of degree $q=2$ from given cell averages to solve the ***Sub-problem 2***.

Let (x_i,y_i) be the coordinates of the barycenter of cell $\mathcal{K}_i$. We use the following monomial expression of a second degree polynomial $P_i(x,y)$ supported on $\mathcal{K}_i$:

$$P_i(x,y)=a_{0,i}+a_{1,i}(x-x_i)+a_{2,i}(y-y_i)+a_{3,i}(x-x_i)^2+a_{4,i}(x-x_i)(y-y_i)+a_{5,i}(y-y_i)^2. \quad (3.20)$$

To reconstruct a polynomial function approximation to a function $v(x,y)$ on cell $\mathcal{K}_i$ from cell average values $\overline{v}_i$ of $v(x,y)$, we also follow the reconstruction algorithm described in Section 3.1 without using *Step 4* and *Step 5*. Moreover in *Step 2* of the algorithm, we use cell average values here for solving the ***Sub-problem 2***; and we do not require the reconstructed $\widetilde{P}_i(x,y)$ to be divergence-free.

For the self-completeness of the paper, we briefly describe the WENO reconstruction of the second degree polynomial $\widetilde{P}_0(x,y)$ (or the third-order accurate reconstruction) on cell $\mathcal{K}_0$. We refer to [21, 22, 26] for description of the first degree polynomial reconstruction. See Fig. 7 for all stencils used in the second degree polynomial reconstruction. On each of the stencil $T^{(m)}, m=1,\cdots,7$, we first reconstruct preliminarily a polynomial $P_0^{(m)}(x,y)$ supported on $\mathcal{K}_0$ by solving a system of linear equations (or a constrained least square problem) respectively.

The central stencil $T^{(1)}$ to reconstruct preliminarily a second degree polynomial $P_0^{(1)}(x,y)$ on cell $\mathcal{K}_0$ is shown in Fig. 7(a). $T^{(1)}$ consists of cell $\mathcal{K}_0$, its three neighbors $\mathcal{K}_1$, $\mathcal{K}_2$ and $\mathcal{K}_3$, and $\mathcal{K}_{s0}$ and $\mathcal{K}_{s1}$ which are two neighbors of $\mathcal{K}_s$ (other than $\mathcal{K}_0$), s=1,2,3. Thus $T^{(1)}=\{\mathcal{K}_0,\mathcal{K}_s,\mathcal{K}_{s0},\mathcal{K}_{s1},s=1,2,3\}$, which consists of the level-1 von Neumann neighbors of $\mathcal{K}_0$ and $\mathcal{K}_0$ itself. The coefficients of $P_0^{(1)}(x,y)$ are determined by solving the following constrained linear problem

$$\begin{cases} \displaystyle\int_{\mathcal{K}_{sl}} P_0^{(1)}(x,y)dxdy=|\mathcal{K}_{sl}|\overline{v}_{sl}, \quad s=1,2,3; \quad l=0,1; \\ \text{subject to:} \\ \displaystyle\int_{\mathcal{K}_{s'}} P_0^{(1)}(x,y)dxdy=|\mathcal{K}_{s'}|\overline{v}_{s'}, \quad s'=0,1,2,3, \end{cases} \quad (3.21)$$

where $|\mathcal{K}|$ is the area of cell $\mathcal{K}$; $\overline{v}_{sl}$ is the cell average value defined on cell $\mathcal{K}_{sl}$; and $\overline{v}_{s'}$ is the cell average value defined on $\mathcal{K}_{s'}$.

https://doi.org/10.4208/cicp.050814.040915a Published online by Cambridge University Press

Within three forward sectors FS_s, $s=1,2,3$, we construct three one-sided stencils $T^{(2)}$, $T^{(3)}$ and $T^{(4)}$ respectively. See Fig. 7(b). In FS_1, $T^{(2)}=\{\mathcal{K}_0,K_3,K_{30},\mathcal{K}_{31},\mathcal{K}_4,\mathcal{K}_5\}$. Thus $T^{(2)}$ consists of $\mathcal{K}_0$, level-1 von Neumann neighbors of $\mathcal{K}_0$ in this sector, and two additional cells $\mathcal{K}_4$ and $\mathcal{K}_5$ which are neighbors of level-1 von Neumann neighbors in this sector (other than $\mathcal{K}_3$). The other two one-sided stencils $T^{(3)}$ and $T^{(4)}$ are constructed similarly.

Then by using every stencil $T^{(m)}$,$m=2,3,4$, we reconstruct preliminarily polynomials $P_0^{(m)}(x,y)$ respectively by solving the following linear system

$$\int_{\triangle_s\left(T^{(m)}\right)} P_0^{(m)}(x,y)dxdy=|\triangle_s(T^{(m)})|\overline{v}_s,\quad s=1,\cdots,6, \tag{3.22}$$

where $\triangle_s(T^{(m)})\in T^{(m)}$ is a cell in $T^{(m)}$, m=2,3,4; $\overline{v}_s$ is the cell average defined on $\triangle_s(T^{(m)})$, and $|\triangle_s(T^{(m)})|$ is the cell area of $\triangle_s(T^{(m)})$.

See Fig. 7(c). Within three backward sectors BS_s, $s=1,2,3$, we construct three reverse-sided stencils $T^{(5)}$, $T^{(6)}$ and $T^{(7)}$ respectively.

In BS_1, $T^{(5)}=\{\mathcal{K}_0,\mathcal{K}_4,\mathcal{K}_{40},\mathcal{K}_{41},\mathcal{K}_5,\mathcal{K}_{50},\mathcal{K}_{51}\}$. The method to construct this stencil is the same as the one used to construct the stencil $T_B^{(5)}$ used to reconstruct a third order accurate divergence-free magnetic field $\mathbf{B}^{xy,(5)}$ described in Appendix A. Stencils $T^{(6)}$ and $T^{(7)}$ are constructed similarly.

We next reconstruct preliminarily polynomial $P_0^{(5)}$ by using stencil $T^{(5)}$ by solving the following constrained least square problem

$$\begin{aligned}&\left\{\int_{\mathcal{K}_l} P_0^{(5)}(x,y)dxdy=|\mathcal{K}_l|\overline{v}_l,\quad l=4,5,40,41,50,51;\right.\\&\text{subject to:}\\&\left\{\int_{\mathcal{K}_0} P_0^{(5)}(x,y)dxdy=|\mathcal{K}_0|\overline{v}_0.\right.\end{aligned} \tag{3.23}$$

Polynomials $P_0^{(6)}(x,y)$ reconstructed by using $T^{(6)}$ and $P_0^{(7)}(x,y)$ reconstructed by using $T^{(7)}$ are computed similarly.

For each $P_0^{(m)}(x,y)$, $m=1,\cdots,7$, we compute a smoothness indicator [22] by

$$SI(P_0^{(m)})=\left(\sum_{|\alpha=1|}\int_{\mathcal{K}_0} h^{-2}(D^\alpha P_0^{(m)}(x,y))^2dxdy\right)^{1/2}. \tag{3.24}$$

This smoothness indicator is suitable for stringent shock wave interaction problems. See [22] for discussion of other oscillation indicators.

Weights ω_m from these smoothness indicators are redefined by

$$\omega_m=\frac{b_m\left(\epsilon+SI(P_0^{(m)})\right)^{-4}}{\sum_{l=1}^7 b_l\left(\epsilon+SI(P_0^{(l)})\right)^{-4}}, \tag{3.25}$$

https://doi.org/10.4208/cicp.050814.040915a Published online by Cambridge University Press

where $b_m=10$ when $m=1$ and $b_m=1$ otherwise. $\epsilon=10^{-6}$ is used to avoid division by zero.

The final nonlinear WENO reconstruction polynomial $\widetilde{P}_0(x,y)$ is defined by

$$\widetilde{P}_0(x,y)=\sum_{m=1}^{7}\omega_m P_0^{(m)}(x,y). \tag{3.26}$$

This completes the third-order accurate reconstruction for approximating $v(x,y)$ on $\mathcal{K}_0$. In the present paper, this reconstruction algorithm is applied at the end of every Runge-Kutta stage, and used to reconstruct every component of $\mathbf{U}^H$ with $\overline{v}_i$ replaced by the cell average values of corresponding component of $\mathbf{U}^H$ computed by the base finite volume scheme.

4 Numerical test problems

4.1 Vortex evolution problem

We consider a vortex evolution problem, which was initially suggested in [7], to assess the convergence order of the scheme.

The problem is defined on a $[-5,5]\times[-5,5]$ domain with periodic boundary conditions on both sides. The unperturbed MHD flow is given by $(\rho,p_{gas},u_x,u_y,B_x,B_y)=(1,1,1,1,0,0)$. The ratio of specific heats is $\gamma=5/3$. The vortex is introduced through perturbed velocity and magnetic fields given by

$$(\delta u_x,\delta u_y)=\frac{\kappa}{2\pi}e^{0.5(1-r^2)}(-y,x),\qquad (\delta B_x,\delta B_y)=\frac{\mu}{2\pi}e^{0.5(1-r^2)}(-y,x),$$

where $r^2=x^2+y^2$. The pressure determined by the dynamical balance is given by

$$\delta p_{gas}=\frac{\kappa^2(1-r^2)-\mu^2}{8\pi^2}e^{1-r^2}.$$

We use $\kappa=1$, $\mu=1$ in our computation. The exact solution is the initial configuration propagating with speed $(1,1)$, and is given by

$$U(x,y,t)=U_0(x-t,y-t).$$

The periodic boundary condition introduces an error of magnitude $\mathcal{O}(10^{-6})$, which does not affect the reported results. The typical triangle edge length, denoted by h, is listed in the first column of all the tables shown in this section. L_1 and L_∞ errors and orders of accuracy of variables ρ and ε at time $T=1.0$ are shown in Table 1 for the second-order accurate divergence-free WENO reconstruction-based scheme and in Table 2 for the third-order accurate scheme. Table 3 shows the L_1 and L_∞ errors and orders of accuracy of x-component of the magnetic field computed by the second- and third-order accurate schemes, respectively. As can be seen, results in these tables show clearly that we have achieved the expected accuracy property of the scheme. The absolute value of the undivided divergence of the magnetic field is about $\mathcal{O}(10^{-13})$ in these simulations.

https://doi.org/10.4208/cicp.050814.040915a Published online by Cambridge University Press

Table 1: Numerical errors and convergence order for the second-order accurate divergence-free WENO reconstruction-based method for solving the 2D vortex evolution problem.

h	L_1 ρ error	order	L_∞ ρ error	order	L_1 ε error	order	L_∞ ε error	order
1/4	2.93E-3	-	7.65E-3	-	1.07E-1	-	3.69E-2	-
1/8	8.22E-3	1.83	4.61E-3	0.73	2.71E-2	1.98	1.42E-2	1.38
1/16	1.38E-3	2.57	1.31E-3	1.81	4.95E-3	2.46	4.84E-3	1.55
1/32	2.40E-4	2.53	3.92E-4	1.74	9.23E-4	2.42	1.71E-3	1.49

Table 2: Numerical errors and convergence order for ρ and ε of the third-order accurate divergence-free WENO reconstruction-based method for solving the 2D vortex evolution problem.

h	L_1 ρ error	order	L_∞ ρ error	order	L_1 ε error	order	L_∞ ε error	order
1/2	2.01E-2	-	2.80E-3	-	1.31E-1	-	2.49E-2	-
1/4	2.31E-3	3.12	4.96E-4	2.50	1.03E-2	3.67	2.44E-3	3.36
1/8	1.85E-4	3.64	4.44E-5	3.48	6.64E-4	3.96	2.03E-4	3.59
1/16	2.58E-5	2.84	8.75E-6	2.34	9.26E-5	2.84	1.90E-5	3.42

Table 3: Numerical errors and convergence order for B_x of the divergence-free WENO reconstruction-based method for solving the 2D vortex evolution problem.

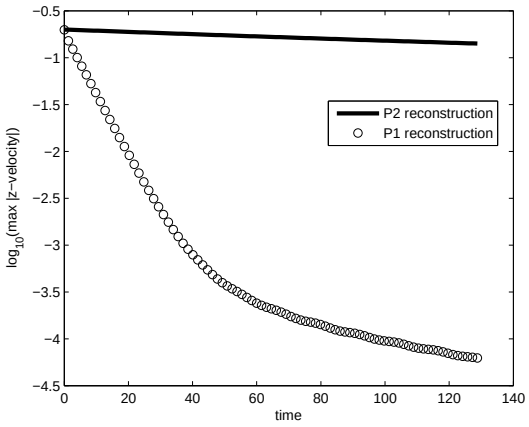
h	second-order case				third-order case			
	L^1 error	L^1 order	L^∞ error	L^∞ order	L^1 error	L^1 order	L^∞ error	L^∞ order
$\frac{1}{2}$	3.06E-1	–	5.07E-2	–	1.25E-1	–	2.42E-2	–
$\frac{1}{4}$	6.12E-2	2.32	1.29E-2	1.97	8.04E-3	3.95	1.89E-3	3.68
$\frac{1}{8}$	1.06E-2	2.53	2.93E-3	2.14	7.69E-4	3.39	1.46E-4	3.69
$\frac{1}{16}$	2.06E-3	2.36	9.10E-4	1.69	1.23E-4	2.64	2.24E-5	2.70

4.2 Numerical dissipation and long-term decay of Alfvén waves

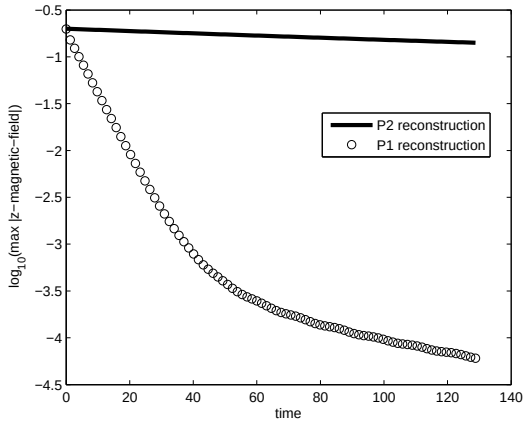
We consider a smooth solution problem proposed in [7], which examines the numerical dissipation of torsional Alfvén waves that are made to propagate at a small angle to the y-axis. We use the same angle $\alpha=\tan(1/6)=9.462^0$; and the magnetic field is normalized by a $1/\sqrt{4\pi}$ factor. The density $\rho_0=1$, and pressure $p_0=1$ are initial values of density and pressure respectively. The unperturbed velocity is $u_0=0$, and the unperturbed magnetic field is $B_0=1$.

The computational domain is $[-r/2,r/2]\times[-r/2,r/2]$ with $r=6$. The direction of wave propagation is along the unit vector $\mathbf{n}\equiv(n_x,n_y)=(\frac{1}{\sqrt{r^2+1}},\frac{r}{\sqrt{r^2+1}})$. The phase of the wave is taken to be $\phi=\frac{2\pi}{n_y}(n_x x+n_y y-V_A t)$, where $V_A=B_0\sqrt{\rho_0}$. The velocity is given by $\mathbf{u}=(u_0 n_x-\epsilon n_y\cos\phi,\ u_0 n_y+\epsilon n_x\cos\phi,\ \epsilon\sin\phi)$, where $\epsilon=0.2$. The magnetic field is given

https://doi.org/10.4208/cicp.050814.040915a Published online by Cambridge University Press



(a)



(b)

Figure 3: (a) Logarithm plot of the maximum of absolute value of the z-component of the velocity from the torsional Alfvén waves propagation problem. (b) Logarithm plot of the maximum of the absolute value of the z-component of the magnetic field from the torsional Alfvén waves propagation problem. The maximum value should remain constant for the exact solution but decay due to the numerical dissipation. The solid line is for the third order accurate scheme; while the circled line is for the second order accurate scheme.

by $\mathbf{B}=(B_0 n_x+\epsilon n_y\sqrt{\rho_0}\cos\phi,\ B_0 n_y-\epsilon n_x\sqrt{\rho_0}\cos\phi,\ -\epsilon\sqrt{\rho_0}\sin\phi)$.

The typical edge length of triangles is roughly equal to $\frac{1}{20}$. Solution of the problem is computed to a time $T=129$. The maximum values of u_z and B_z should remain constant over time for the exact solution, but decay due to the numerical dissipation. Therefore this problem provides a good assessment of dissipation of the numerical scheme. Fig. 3 shows the logarithm of the maximum of absolute values of u_z and B_z over time. We see clearly that the third order accurate scheme is substantially less dissipative than the second order accurate scheme.

https://doi.org/10.4208/cicp.050814.040915a Published online by Cambridge University Press

In what follows, we test the problems with discontinuities to assess the non-oscillatory property of the proposed third order accurate scheme.

4.3 Rotor problem

This test problem is first proposed in [5] and is considered as the second rotor problem in [42]. The computational domain is $[0,1]\times[0,1]$. $\gamma=5/3$. A dense rotating disk of fluid is initially placed at the central area of the computational domain, while the ambient fluid is at rest. The initial condition is given by

$$(\rho,p_{gas},u_x,u_y,u_z,B_x,B_y,B_z)=\left(\rho(\mathbf{x},0),0.5,u_x(\mathbf{x},0),u_y(\mathbf{x},0),0,\frac{2.5}{\sqrt{4\pi}},0,0\right).$$

Here

$$(\rho(\mathbf{x},0),u_x(\mathbf{x},0),u_y(\mathbf{x},0))=\begin{cases}10, & -(y-0.5)/r_0, & (x-0.5)/r_0 & \text{if } r<r_0,\\ 1+9f, & -(y-0.5)f/r, & (x-0.5)f/r & \text{if } r_0<r<r_1,\\ 1, & 0, & 0, & \text{if } r>r_1,\end{cases}$$

where $r_0=0.1$, $r_1=0.115$, $f=(r_1-r)/(r_1-r_0)$, and $r=\sqrt{(x-0.5)^2+(y-0.5)^2}$.

The solution at time $t=0.295$ is computed. The typical edge length of triangles used to partition the domain is about $\frac{1}{150}$. A CFL number 0.4 is used for calculation. Fig. 4 plots the numerical result of the density ρ, pressure p_{gas}, magnetic pressure $(B_x^2+B_y^2)/2$ and Mach number. We see that there is virtually no diffusion of the loop's boundaries and no oscillations in the magnetic pressure within the loop's interior. The pressure is positive throughout the computational domain. The degradation in the density variable that was previously reported in [31] is not seen in our simulation.

4.4 Blast wave problem

This test problem is taken from [5]. It was about a spherical strong fast magneto-sonic shock propagates through a low-β (β = 0.000251) ambient plasma. We use it to show the advantages of the divergence-free reconstruction. The setup of the problem is as follows: on a computational domain $[0,1]\times[0,1]$, $\rho=1$, $\mathbf{u}=0$, $B_x=50/\sqrt{4\pi}$, $B_y=B_z=0$, $p_{gas}=1000$ within a circle centered at $(0.5,0.5)$ of radius $R=0.1$ and $p_{gas}=1.0$ elsewhere. The final simulation time $t=0.01$. The typical edge length of triangles used to partition the domain is about 0.0075. This is a stringent test problem [5]. The pressure is several orders of magnitude smaller than the magnetic energy. A small discretization error in the total energy can produce negative pressure near the shock front, as observed by others [28,30]. We used local divergence-free reconstruction to treat this. Briefly, if after reconstructing the magnetic field on a cell, the pressure computed from cell average values may become negative at quadrature points of cells near the shock, we try to use a simple scaling technique introduced in [43,47,48] to remove the negative pressure. In these papers, we show

https://doi.org/10.4208/cicp.050814.040915a Published online by Cambridge University Press

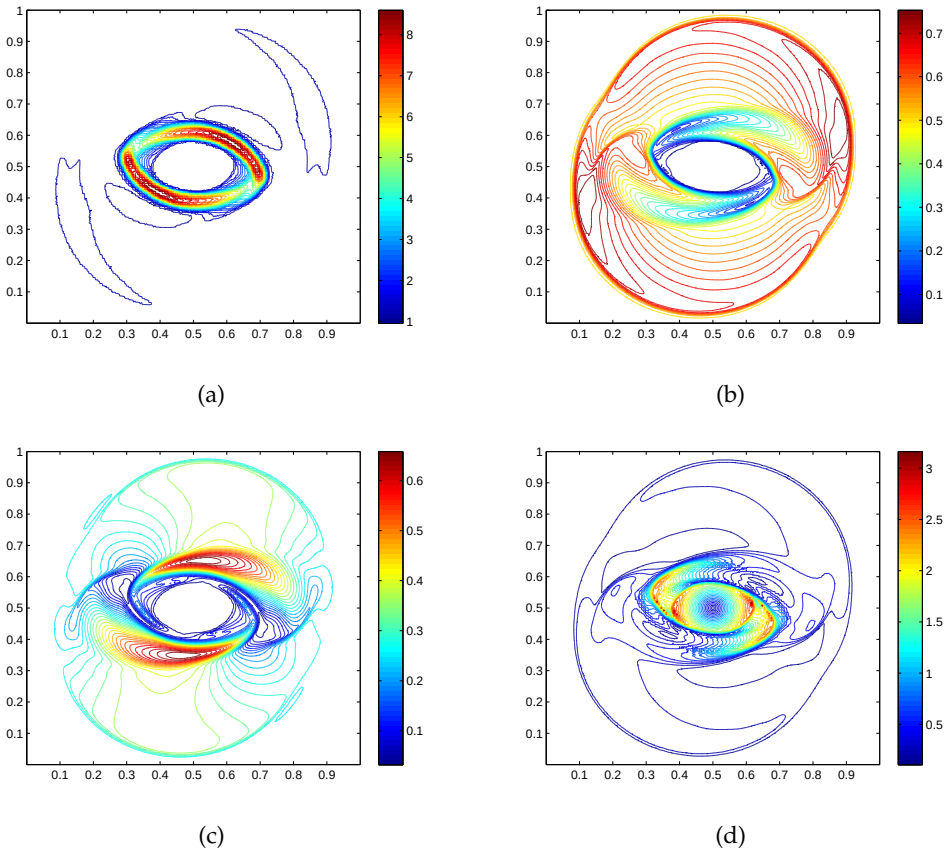


Figure 4: P^2 solution of the rotor problem at time $t=0.295$. Thirty equally spaced contours are shown in each plot. (a) Density ρ; (b) pressure p_{gas}; (c) magnetic pressure $(B_x^2+B_y^2)/2$; (d) Mach number.

how order can be reduced to retrieve the positivity property. It is also shown that this can be done while preserving the locally divergence-free property for the magnetic field.

Fig. 5 plots the numerical result of the density ρ, pressure p_{gas}, magnetic pressure $(B_x^2+B_y^2)/2$ and magnitude of the velocity $\sqrt{u_x^2+u_y^2}$. Owing to the large pressure placed at the center of the domain at the start of calculation, a strong blast wave propagates outwards, leaving a low density region in the center of the computational domain. We see that there is only minor oscillations in the density plot. Other fields are resolved nicely.

4.5 Orszag-Tang problem

Here we simulate the Orszag-Tang vortex problem [33]. The initial conditions are $u_x=-\sin(y)$, $u_y=\sin(x)$, $B_x=-\sin(y)$, $B_y=\sin(2x)$, $\rho=\gamma^2$, $p_{gas}=\gamma$, $u_z=B_z=0$. The computational domain is a square $[0,2\pi]\times[0,2\pi]$ with periodic boundary conditions along

https://doi.org/10.4208/cicp.050814.040915a Published online by Cambridge University Press

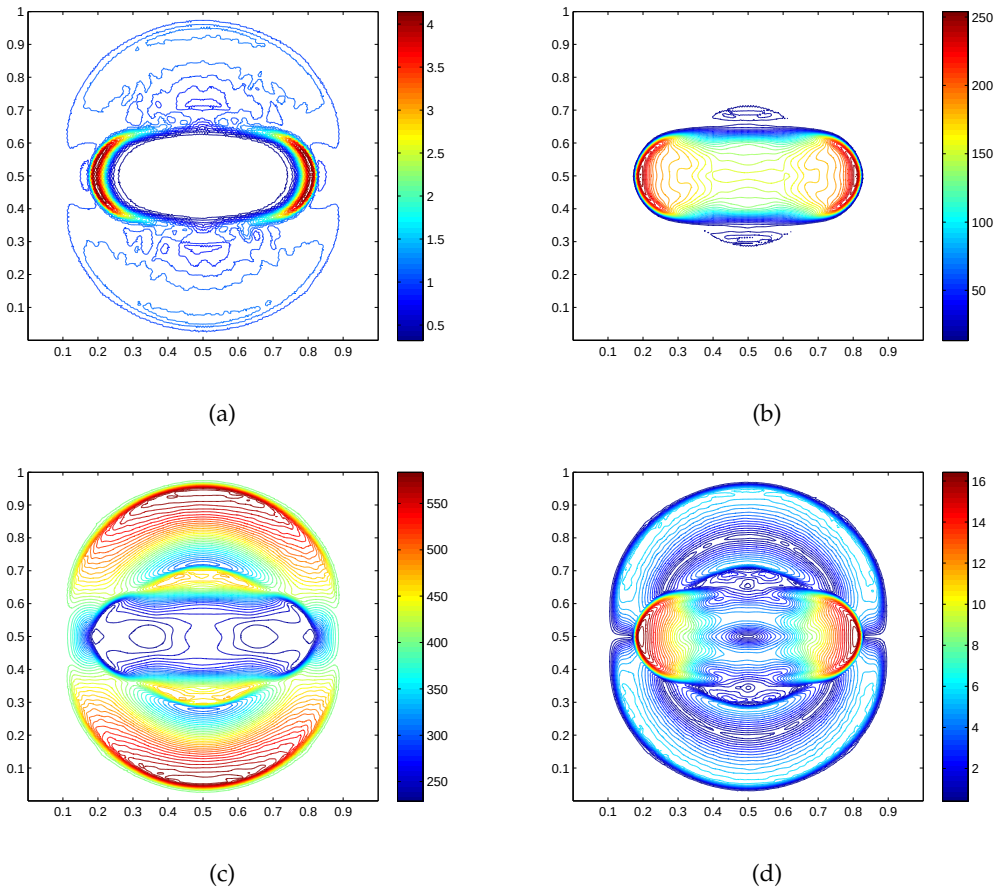


Figure 5: P^2 solution of the blast wave problem at time $t=0.01$. Forty equally spaced contours are shown in each plot. (a) Density ρ; (b) pressure p_{gas}; (c) magnetic pressure $(B_x^2+B_y^2)/2$; (d) Magnitude of the velocity $\sqrt{u_x^2+u_y^2}$.

both boundaries. $\gamma=5/3$. The final output time $t=\pi$. The typical edge length of triangles used to partition the domain is about $\frac{1}{256}$. Starting from a smooth initial condition, the flow becomes very complex as expected from a transition towards turbulence gradually. Fig. 6 shows the development of density ρ in the Orszag-Tang vortex problem. Also we report that the density and pressure have remained positive. No positivity fix was needed for this problem.

5 Concluding remarks

In this paper we introduced a divergence-free WENO reconstruction-based finite volume method for solving the ideal MHD equations on two-dimensional triangular grids. The

https://doi.org/10.4208/cicp.050814.040915a Published online by Cambridge University Press

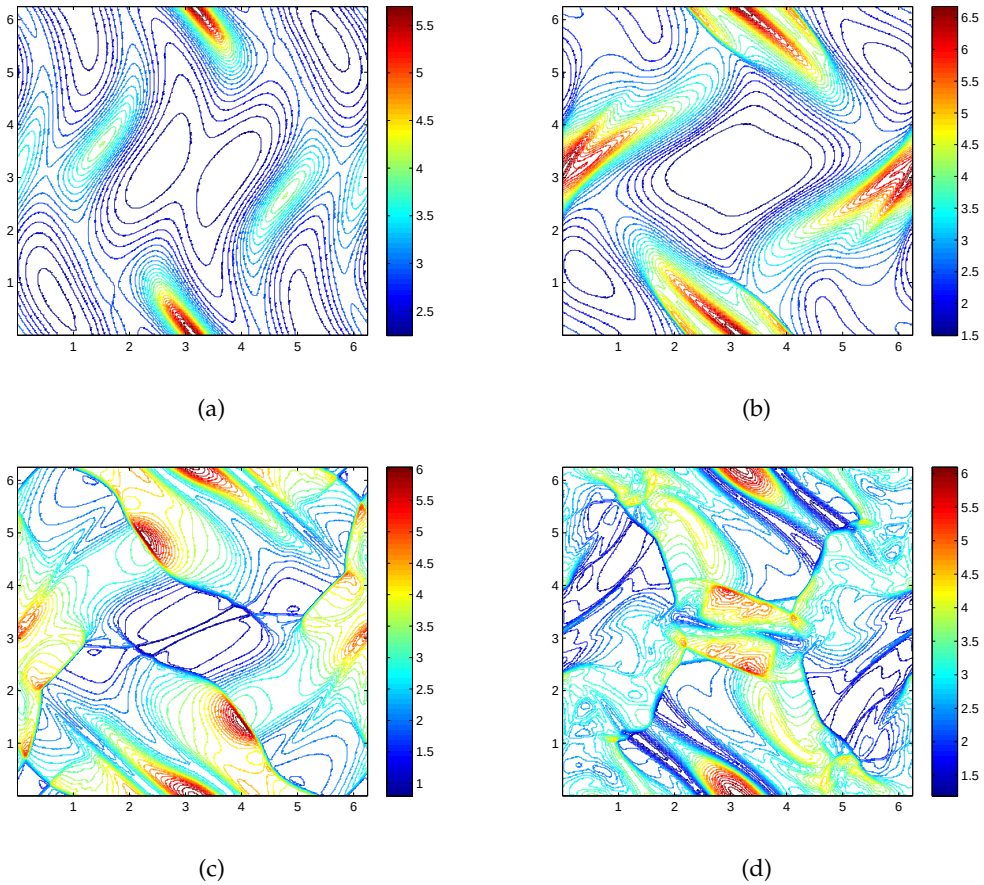


Figure 6: Orszag-Tang problem. Evolution of ρ over time. Top left: $t=0.5$; top right: $t=1.0$; bottom left: $t=2.0$; bottom right: $t=3.14$. 15 equally spaced contours are used.

proposed method is based on the CT framework and achieves exactly divergence-free magnetic field. Numerical tests show that the proposed schemes have achieved the desired order of accuracy and the third order accurate scheme has been shown to perform very well for shock wave problems. We will report in a subsequent paper a multidimensional HLL/HHLC Riemann solver to resolve this issue. While this paper only implements the second- and third-order accurate schemes, the proposed method in principle can be generalized to three dimensions and to general meshes.

Acknowledgments

Research was partially supported by the National Science Foundation grants DMS-1115887 and AST-1009091.

https://doi.org/10.4208/cicp.050814.040915a Published online by Cambridge University Press

Appendix

A.1 Third-order accurate reconstruction for $\mathbf{B}^{xy}$

The third-order accurate divergence-free reconstruction of $\mathbf{B}^{xy}$ on cells is a straight forward extension of the second-order accurate reconstruction described in Section 3.2. Thus we catalogue the key steps in implementing the third-order accurate case in this subsection.

To avoid introducing too many notations, representation of the preliminarily reconstructed $\mathbf{B}^{xy,(m)}=\left(B_x^{(m)},B_y^{(m)}\right)^T$ is redefined by the following quadratic polynomial expression

$$\begin{aligned} B_x^{(m)}(x,y)&=a_{0,m}+a_{1,m}x+a_{2,m}y+a_{3,m}x^2+a_{4,m}xy+a_{5,m}y^2,\\ B_y^{(m)}(x,y)&=b_{0,m}+b_{1,m}x+b_{2,m}y+b_{3,m}x^2+b_{4,m}xy+b_{5,m}y^2. \end{aligned} \tag{A.1}$$

The subscript "i" of cell indices is also dropped for convenience. We note that the preliminarily reconstructed $\widetilde{\mathbf{B}}_i^{xy,(m)}$, WENO combined $\widetilde{\mathbf{B}}_i^{xy}$ and reconstructed $\widetilde{\widetilde{\mathbf{B}}}_i^{xy}$ supported on cell $\mathcal{K}_i\in\mathcal{T}_h$, all belong to $\{\mathbf{v}\in P_2(\mathcal{K}_i)^2:\nabla\cdot\mathbf{v}=0\}$.

The divergence-free condition $\nabla\cdot\mathbf{B}^{xy,(m)}=0$ for the third-order accurate reconstruction gives the following three equations

$$\begin{aligned} &a_{1,m}+b_{2,m}=0,\\ &2a_{3,m}+b_{4,m}=0,\\ &a_{4,m}+2b_{5,m}=0 \end{aligned} \tag{A.2}$$

by matching coefficients. This reduces three of the degrees of freedom in preliminarily reconstructing the third-order accurate $\mathbf{B}^{xy,(m)}$.

Fig. 7 shows stencils used for the third-order accurate divergence-free reconstruction. The central stencil is shown in Fig. 7(a). Fig. 7(b) shows three forward sectors FS_s, $s=1,2,3$ and cells in these forward sectors used to construct one-sided stencils. For the convenience, we still denote the one-sided stencil in BS_1 by $T_B^{(2)}$, the one in BS_2 by $T_B^{(3)}$ and the one in BS_3 by $T_B^{(4)}$. Fig. 7(c) shows three backward sectors BS_s, $s=1,2,3$ and cells in these backward sectors used to construct corresponding reverse-sided stencils. Similarly, the reverse-sided stencil in BS_1 is denote by $T_B^{(5)}$, the one in BS_2 by $T_B^{(6)}$ and the one in BS_3 by $T_B^{(7)}$. The details of constructing these stencils and reconstructing polynomial $\mathbf{B}^{xy,(m)}$ are given below.

A.1.1 Preliminary third-order accurate reconstruction on central stencil

See Fig. 7(a). The central stencil $T_B^{(1)}$ of $\mathcal{K}_0$ contains cells in level-1 von Neumann neighbors of $\mathcal{K}_0$ and $\mathcal{K}_0$ itself. On cell $\mathcal{K}_0$, we arbitrarily choose two cell edge-length-averaged values of normal components of $\mathbf{B}^{xy}$. On each of the remaining cells, we choose one

https://doi.org/10.4208/cicp.050814.040915a Published online by Cambridge University Press

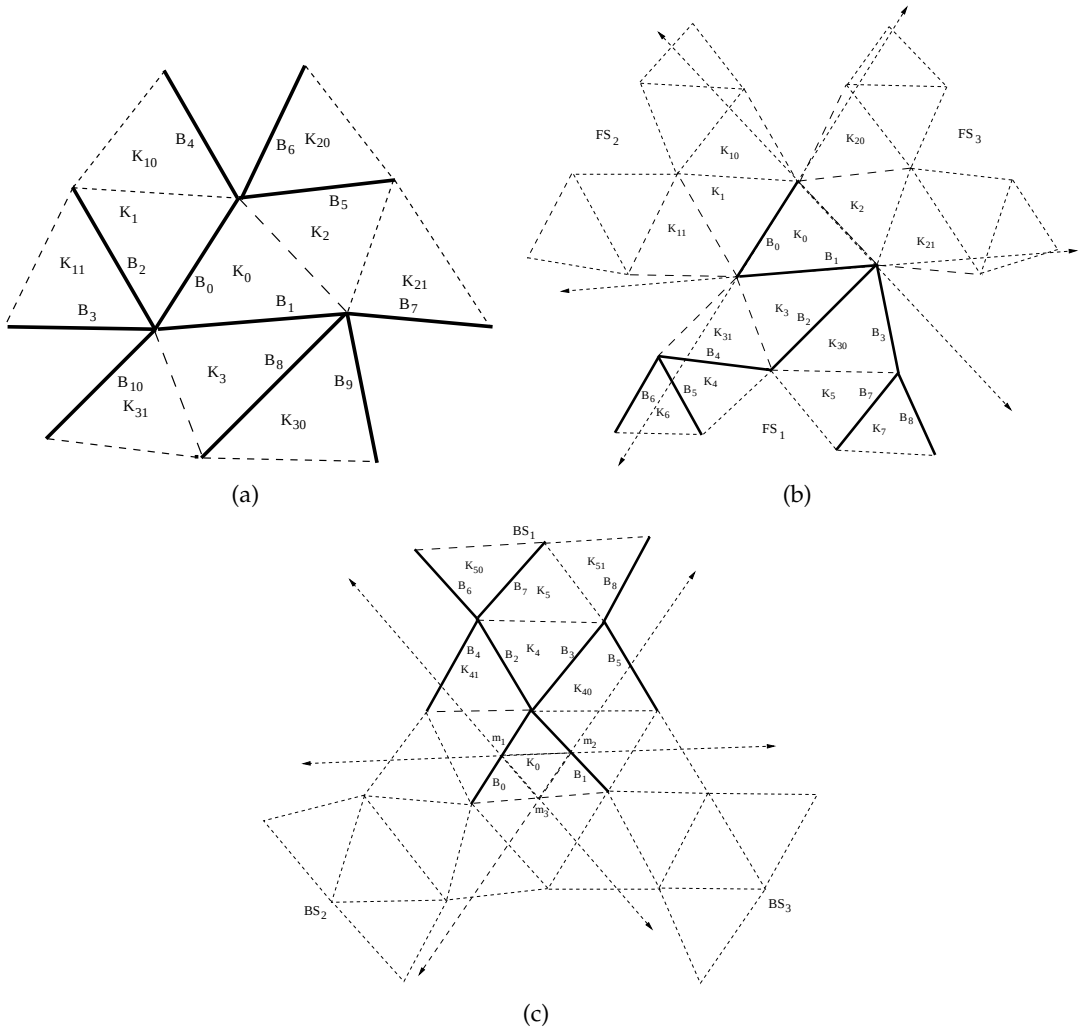


Figure 7: Stencils for reconstructing the third-order accurate cell-centered divergence-free magnetic field as well as for reconstructing the third-order accurate polynomial approximations for cell centered variables on cell $\mathcal{K}_0$. To reconstruct the divergence-free magnetic field, normal components of the magnetic field on solid line edges are utilized. (a) The central stencil, (b) Three forward sectors FS_1, FS_2 an FS_3 of cell $\mathcal{K}_0$ formed by spanning a pair of edges of $\mathcal{K}_0$ respectively. The cells of three one-sided stencils formed in each of the forward sectors are shown here. (c) Three backward sectors BS_1, BS_2 and BS_3 of $\mathcal{K}_0$. A backward sector is defined by having its origin at the midpoint of an edge of $\mathcal{K}_0$ and its two boundary edges passing through the other two midpoints of remaining edges of $\mathcal{K}_0$. The cells of three reverse-sided stencils formed in each of the backward sectors are shown here. *Note that the same notations are used for different normal components of the magnetic field and cells in (a), (b) and (c) to avoid introducing too many notations.*

edge-length-averaged values on the edge which is connected to one of vertices of $\mathcal{K}_0$. We relabel these average values by $\{B_s : s=0,\cdots,10\}$. We then solve the following system of linear equations with linear constraints to obtain $\mathbf{B}^{xy,(1)}$

https://doi.org/10.4208/cicp.050814.040915a Published online by Cambridge University Press

$$\left\{ \frac{1}{|\mathcal{L}_s|}\int_{\mathcal{L}_s}\mathbf{B}^{xy,(m)}\cdot\mathbf{n}_s d\zeta = B_s, \quad s=2,\cdots,10, \right. \tag{A.3}$$

subject to:

$$\begin{cases} a_{1,m}+b_{2,m}=0, \\ 2a_{3,m}+b_{4,m}=0, \\ a_4+2b_5=0, \\ \dfrac{1}{|\mathcal{L}_{s'}|}\displaystyle\int_{\mathcal{L}_{s'}}\mathbf{B}^{xy,(m)}\cdot\mathbf{n}_{s'}d\zeta = B_{s'}, \quad s'=0,1. \end{cases} \tag{A.4}$$

Here $m=1$. We remark that when solving this system given by (A.3)-(A.4), Eq. (A.4) is satisfied exactly; while Eq. (A.3) is satisfied in the least square sense. Similar to the second-order accurate preliminary reconstruction on reverse-sided stencil, Eq. (A.2) is substituted into Eq. (A.3) before solving (A.3)-(A.4). The system (A.3)-(A.4) make sures that the preliminarily reconstructed magnetic field $\mathbf{B}^{xy,(1)}$ on $\mathcal{K}_0$ is divergence-free, and matches the mean values of the magnetic field defined on the cell edges enclosing $\mathcal{K}_0$ exactly.

A.1.2 Preliminary third-order accurate reconstruction on one-sided stencils

Within each of the forward sectors, we construct an one-sided stencil. See Fig. 7(b). Take the one-sided stencil $T_B^{(2)}$ constructed in the forward sector FS_1 for example. $T_B^{(2)}$ contains cells in level-3 von Neumann neighbors of $\mathcal{K}_0$, which are close to the edges of FS_1, and $\mathcal{K}_0$ itself. Thus $T_B^{(2)}=\{\mathcal{K}_0,\mathcal{K}_3,\mathcal{K}_{30},\mathcal{K}_{31},\mathcal{K}_4,\mathcal{K}_5,\mathcal{K}_6,\mathcal{K}_7\}$. One-sided stencils $T_B^{(3)}$ and $T_B^{(4)}$ are constructed similarly.

To reconstruct quadratic polynomial $\mathbf{B}^{xy,(2)}$ on $\mathcal{K}_0$ by using $T_B^{(2)}$, we choose two cell edge-length-averaged values of normal components of $\mathbf{B}^{xy}$ with one of them defined on the edge shared by cells $\mathcal{K}_0$ and $\mathcal{K}_3$ (level-0 von Neumann neighbor). Then we choose 7 edge values from the remaining cells. The solid line edges shown in Fig. 7(b) give one admissible selection of these 7 edge values. We relabel these edge-length-averaged values by $\{B_s : s=0,\cdots,8\}$. Then the following linear problem is solved to reconstruct preliminarily a candidate $\mathbf{B}^{xy,(2)}$

$$\begin{cases} a_{1,m}+b_{2,m}=0, \\ 2a_{3,m}+b_{4,m}=0, \\ a_{4,m}+2b_{5,m}=0, \\ \dfrac{1}{|\mathcal{L}_s|}\displaystyle\int_{\mathcal{L}_s}\mathbf{B}^{xy,(m)}\cdot\mathbf{n}_s d\zeta = B_s, \quad s=0,\cdots,8. \end{cases} \tag{A.5}$$

Here $m=2$. The other two preliminarily reconstructed polynomials $\mathbf{B}^{xy,(3)}$ by using $T_B^{(3)}$ and $\mathbf{B}^{xy,(4)}$ by using $T_B^{(4)}$ are computed in the same manner.

https://doi.org/10.4208/cicp.050814.040915a Published online by Cambridge University Press

A.1.3 Preliminary third-order accurate reconstruction on reverse-sided stencils

See Fig. 7(c). The reverse-sided stencils are constructed in the backward sectors respectively. Take the reverse-sided stencil $T_B^{(5)}$ constructed in the backward sector BS_1 for example. $T_B^{(5)}$ contains two level-1 von Neumann neighbors $\mathcal{K}_{41}$ and $\mathcal{K}_{40}$, one level-2 von Neumann neighbor $\mathcal{K}_4$ which is adjacent to both $\mathcal{K}_{41}$ and $\mathcal{K}_{40}$, one level-3 von Neumann neighbor $\mathcal{K}_5$ which is adjacent to $\mathcal{K}_4$ and two level-4 von Neumann neighbors $\mathcal{K}_{50}$ and $\mathcal{K}_{51}$ which are adjacent to $\mathcal{K}_5$ (other than $\mathcal{K}_4$). The other two reverse-sided stencils $T_B^{(6)}$ and $T_B^{(7)}$ are constructed in the same manner.

To reconstruct the quadratic polynomial $\mathbf{B}^{xy,(5)}$ supported on $\mathcal{K}_0$ by using stencil $T_B^{(5)}$, we note that there are also multiple approaches to select cell edge-length-averaged values of normal component of $\mathbf{B}^{xy}$. Fig. 7(c) shows one choice. Normal components of $\mathbf{B}^{xy}$ defined on the solid line edges in stencil $T_B^{(5)}$ are utilized. We choose two cell edge-length-averaged values of normal components of $\mathbf{B}^{xy}$ on two edges of $\mathcal{K}_0$ whose common end point is in the backward sector BS_1. We also choose four cell edge-length-averaged values of normal component of $\mathbf{B}^{xy}$ from edges of $\mathcal{K}_{40}$ and $\mathcal{K}_{41}$, which are level-1 von Neumann neighbors of $\mathcal{K}_0$. We then choose three cell edge-length-averaged values of normal component of $\mathbf{B}^{xy}$ from edges of remaining cells in the stencil.

We relabel these edge-length-averaged values by $\{B_s : s=0,\cdots,8\}$. We then solve the linear problem (A.5) to obtain $\mathbf{B}^{xy,(5)}$ The other two preliminarily reconstructed polynomials $\mathbf{B}^{xy,(6)}$ by using $T_B^{(6)}$ and $\mathbf{B}^{xy,(7)}$ by using $T_B^{(7)}$ are computed in the same manner.

A.1.4 Computation of weights for third-order accurate WENO reconstruction

We now use a weighted combination of $\{\mathbf{B}^{xy,(m)} : m=1,\cdots,7\}$ to finalize $\widetilde{\mathbf{B}}_0^{xy}$ using the idea of WENO [22,40]. Let $\mathbf{B}^{xy,(m)} = \left(B_x^{(m)}(x,y), B_y^{(m)}(x,y)\right)^T$ be expressed by Eq. (A.1).

We first compute smoothness measures [22] of x-component and y-component of $\mathbf{B}^{xy,(m)}$ respectively by

$$SI(B^{(m)}) = \left(\sum_{|\beta|=1} \int_{\mathcal{K}_0} h^{-2} (D^\beta B^{(m)}(x,y))^2 dxdy \right)^{1/2}. \tag{A.6}$$

Here B stands for either $B_x^{(m)}(x,y)$ or $B_y^{(m)}(x,y)$.

The α_m is redefined by

$$\alpha_m = \frac{b_m}{\left(\epsilon + SI(B_x{}^{(m)}) + SI(B_y{}^{(m)})\right)^4}, \quad m=1,\cdots,7.$$

$\epsilon = 10^{-6}$ is used to avoid division by zero. $b_m = 10$ when $m=1$; and $b_m = 1$ otherwise [27].

https://doi.org/10.4208/cicp.050814.040915a Published online by Cambridge University Press

The weight ω_m for the third-order accurate divergence-free reconstruction is computed by

$$\omega_m = \frac{\alpha_m}{\sum_{l=1}^{7}\alpha_l}.$$

Finally, we reconstruct the piecewise quadratic polynomial approximation $\widetilde{\mathbf{B}}_0^{xy}$ on $\mathcal{K}_0$ by

$$\widetilde{\mathbf{B}}_0^{xy} = \sum_{m=1}^{7}\omega_m \mathbf{B}^{xy,(m)}.$$

Notice that $\widetilde{\mathbf{B}}_0^{xy}$ satisfies the divergence-free condition $\nabla\cdot\widetilde{\mathbf{B}}_0^{xy}=0$ as well as Eq. (3.8) exactly. This completes *Step 3* for the third-order accurate divergence-free reconstruction for the magnetic field on $\mathcal{K}_0$.

A.1.5 Third-order accurate reconstruction for $\widetilde{B}_{n,j}$ on cell edges

The method to reconstruct a quadratic and non-oscillatory polynomial approximation to the normal component of the magnetic field $\widetilde{B}_{n,j}$ supported on cell edges for each $\mathcal{L}_j$, $j=1,\cdots,\mathcal{N}_{\mathfrak{E}}$ is identical to the one described in Section 3.2.5 for the linear polynomial approximation. So we briefly outline the steps to reconstruct the quadratic polynomial approximation on the edge in this subsection.

Still using notations introduced in Section 3.2.5, we denote two grid cells sharing $\mathcal{L}_j$ by $\mathcal{K}_i$ and $\mathcal{K}_{i'}$ and the reconstructed magnetic field $\widetilde{\mathbf{B}}_i^{xy}$ and $\widetilde{\mathbf{B}}_{i'}^{xy}$ supported on each of them respectively.

On edge $\mathcal{L}_j$, we represent the normal components of $\widetilde{\mathbf{B}}_i^{xy}$ and $\widetilde{\mathbf{B}}_{i'}^{xy}$ as:

$$\begin{aligned} B_{n,i}(\zeta) &= \hat{a}_j + \hat{b}_i\zeta + \hat{c}_i\Big(\frac{3}{2}\zeta^2-\frac{1}{2}\Big), \\ B_{n,i'}(\zeta) &= \hat{a}_j + \hat{b}_{i'}\zeta + \hat{c}_{i'}\Big(\frac{3}{2}\zeta^2-\frac{1}{2}\Big), \quad -1\le\zeta\le 1, \end{aligned} \tag{A.7}$$

with respect to the edge unit normal $\mathbf{n}_j$ and the parametric Eq. (3.9) of $\mathcal{L}_j$. Notice that $B_{n,i}(\zeta)$ and $B_{n,i'}(\zeta)$ are written as the linear combinations of Legendre polynomials $1,\zeta$ and $\frac{1}{2}(3\zeta^2-1)$. Similar to the linear polynomial reconstruction case, $B_{n,i}(\zeta)$ and $B_{n,i'}(\zeta)$ have the same constant coefficient $\hat{a}_j$, which is equal to $\overline{B_{n,j}}$, and $\hat{b}_i\neq\hat{b}_{i'}$ and $\hat{c}_i\neq\hat{c}_{i'}$ in general.

Finally the reconstructed $\widetilde{B}_{n,j}$ supported on $\mathcal{L}_j$ is computed by

$$\widetilde{B}_{n,j}(\zeta) = \hat{a}_j + \hat{b}_j\zeta + \hat{c}_j\Big(\frac{3}{2}\zeta^2-\frac{1}{2}\Big), \quad -1\le\zeta\le 1, \tag{A.8}$$

where $\hat{b}_j=\text{minmod}(\hat{b}_i,\hat{b}_{i'})$ and $\hat{c}_j=\text{minmod}(\hat{c}_i,\hat{c}_{i'})$.

https://doi.org/10.4208/cicp.050814.040915a Published online by Cambridge University Press

A.1.6 Third-order accurate, non-oscillatory, divergence-free reconstruction for $\widetilde{\widetilde{\mathbf{B}}}_i^{xy}$ with continuous normal component

The last step of the ***algorithm for reconstructing magnetic field*** is to reconstruct a non-oscillatory, divergence-free $\widetilde{\widetilde{\mathbf{B}}}_i^{xy}(x,y)$ with continuous normal component on each cell $\mathcal{K}_i$. Unlike the second-order accurate case, here we need to use reconstructed $\widetilde{B}_{n,\ell_i^{-1}(l)}$, l=1,2,3 on edges of $\mathcal{K}_i$ as well as edge-length-averaged $\overline{B_n}$ from edge-adjacent neighbors of $\mathcal{K}_i$.

See Fig. 7(a) for instance. To reconstruct $\widetilde{\widetilde{\mathbf{B}}}_0^{xy}(x,y)$ on cell $\mathcal{K}_0$, we use: reconstructed $\widetilde{B}_{n,\ell_0^{-1}(l)}$, $l=1,2,3$ on edges of $\mathcal{K}_0$, $\overline{B_{n,2}}$ (denoted by B_2) on an edge of $\mathcal{K}_1$, $\overline{B_{n,5}}$ (denoted by B_5) on an edge of $\mathcal{K}_2$ and $\overline{B_{n,8}}$ (denoted by B_8) on an edge of $\mathcal{K}_3$.

Let $\widetilde{\widetilde{\mathbf{B}}}_0^{xy}=(\widetilde{\widetilde{B}}_x,\widetilde{\widetilde{B}}_y)^T$ be represented by

$$\begin{aligned}\widetilde{\widetilde{B}}_x(x,y)&=\widetilde{\widetilde{a}}_0+\widetilde{\widetilde{a}}_1x+\widetilde{\widetilde{a}}_2y+\widetilde{\widetilde{a}}_3x^2+\widetilde{\widetilde{a}}_4xy+\widetilde{\widetilde{a}}_5y^2,\\ \widetilde{\widetilde{B}}_y(x,y)&=\widetilde{\widetilde{b}}_0+\widetilde{\widetilde{b}}_1x+\widetilde{\widetilde{b}}_2y+\widetilde{\widetilde{b}}_3x^2+\widetilde{\widetilde{b}}_4xy+\widetilde{\widetilde{b}}_5y^2.\end{aligned}\tag{A.9}$$

On each edge $\mathcal{L}_{\ell_0^{-1}(l)}$ of $\mathcal{K}_0$, we represent the normal component $B_{n,\ell_0^{-1}(l)}(\zeta)$ of $\widetilde{\widetilde{\mathbf{B}}}_0^{xy}(x,y)$ by

$$\begin{aligned}&B_{n,\ell_0^{-1}(l)}(\zeta)=\mathbf{n}_{\ell_0^{-1}(l)}\cdot\widetilde{\widetilde{\mathbf{B}}}_0^{xy}(x(\zeta),y(\zeta))\\
=&n_{x,\ell_0^{-1}(l)}\left(\widetilde{\widetilde{a}}_0+\widetilde{\widetilde{a}}_1x_{\ell_0^{-1}(l),m}+\widetilde{\widetilde{a}}_2y_{\ell_0^{-1}(l),m}+\widetilde{\widetilde{a}}_3x^2_{\ell_0^{-1}(l),m}+\widetilde{\widetilde{a}}_4x_{\ell_0^{-1}(l),m}y_{\ell_0^{-1}(l),m}+\widetilde{\widetilde{a}}_5y^2_{\ell_0^{-1}(l),m}\right)\\
&+n_{y,\ell_0^{-1}(l)}\left(\widetilde{\widetilde{b}}_0+\widetilde{\widetilde{b}}_1x_{\ell_0^{-1}(l),m}+\widetilde{\widetilde{b}}_2y_{\ell_0^{-1}(l),m}+\widetilde{\widetilde{b}}_3x^2_{\ell_0^{-1}(l),m}+\widetilde{\widetilde{b}}_4x_{\ell_0^{-1}(l),m}y_{\ell_0^{-1}(l),m}+\widetilde{\widetilde{b}}_5y^2_{\ell_0^{-1}(l),m}\right)\\
&+\Big[n_{x,\ell_0^{-1}(l)}\Big(\widetilde{\widetilde{a}}_1\triangle x_{\ell_0^{-1}(l)}+\widetilde{\widetilde{a}}_2\triangle y_{\ell_0^{-1}(l)}+\widetilde{\widetilde{a}}_32x_{\ell_0^{-1}(l),m}\triangle x_{\ell_0^{-1}(l)}+\\
&\quad+\widetilde{\widetilde{a}}_4(x_{\ell_0^{-1}(l),m}\triangle y_{\ell_0^{-1}(l)}+y_{\ell_0^{-1}(l),m}\triangle x_{\ell_0^{-1}(l)})+\widetilde{\widetilde{a}}_52y_{\ell_0^{-1}(l),m}\triangle y_{\ell_0^{-1}(l)}\Big)\\
&\quad+n_{y,\ell_0^{-1}(l)}\Big(\widetilde{\widetilde{b}}_1\triangle x_{\ell_0^{-1}(l)}+\widetilde{\widetilde{b}}_2\triangle y_{\ell_0^{-1}(l)}+\widetilde{\widetilde{b}}_32x_{\ell_0^{-1}(l),m}\triangle x_{\ell_0^{-1}(l)}\\
&\quad+\widetilde{\widetilde{b}}_4(x_{\ell_0^{-1}(l),m}\triangle y_{\ell_0^{-1}(l)}+y_{\ell_0^{-1}(l),m}\triangle x_{\ell_0^{-1}(l)})+\widetilde{\widetilde{b}}_52y_{\ell_0^{-1}(l),m}\triangle y_{\ell_0^{-1}(l)}\Big)\Big]\zeta\\
&+\Big[n_{x,\ell_0^{-1}(l)}\Big(\widetilde{\widetilde{a}}_3\triangle x^2_{\ell_0^{-1}(l)}+\widetilde{\widetilde{a}}_4\triangle x_{\ell_0^{-1}(l)}\triangle y_{\ell_0^{-1}(l)}+\widetilde{\widetilde{a}}_5\triangle y^2_{\ell_0^{-1}(l)}\Big)\\
&\quad+n_{y,\ell_0^{-1}(l)}\Big(\widetilde{\widetilde{b}}_3\triangle x^2_{\ell_0^{-1}(l)}+\widetilde{\widetilde{b}}_4\triangle x_{\ell_0^{-1}(l)}\triangle y_{\ell_0^{-1}(l)}+\widetilde{\widetilde{b}}_5\triangle y^2_{\ell_0^{-1}(l)}\Big)\Big]\zeta^2\end{aligned}\tag{A.10}$$

by using the parametric equation (3.9) to represent $\mathcal{L}_{\ell_0^{-1}(l)}$.

Next we solve the following system of linear equations with linear constraints for

https://doi.org/10.4208/cicp.050814.040915a Published online by Cambridge University Press

$\widetilde{\widetilde{a}}_0$,$\widetilde{\widetilde{a}}_1$, $\widetilde{\widetilde{a}}_2$,$\widetilde{\widetilde{a}}_3$, $\widetilde{\widetilde{a}}_4$,$\widetilde{\widetilde{a}}_5$, $\widetilde{\widetilde{b}}_0$,$\widetilde{\widetilde{b}}_1$,$\widetilde{\widetilde{b}}_2$, $\widetilde{\widetilde{b}}_3$,$\widetilde{\widetilde{b}}_4$ and $\widetilde{\widetilde{b}}_5$ to reconstruct $\widetilde{\widetilde{\mathbf{B}}}_0^{xy}(x,y)$ supported on $\mathcal{K}_0$

$$\begin{cases} \text{C1}: \dfrac{1}{|\mathcal{L}_2|}\displaystyle\int_{\mathcal{L}_2}\widetilde{\widetilde{\mathbf{B}}}_0^{xy}\cdot\mathbf{n}_2 d\zeta = B_2, \\ \text{C2}: \dfrac{1}{|\mathcal{L}_5|}\displaystyle\int_{\mathcal{L}_5}\widetilde{\widetilde{\mathbf{B}}}_0^{xy}\cdot\mathbf{n}_5 d\zeta = B_5, \\ \text{C3}: \dfrac{1}{|\mathcal{L}_8|}\displaystyle\int_{\mathcal{L}_8}\widetilde{\widetilde{\mathbf{B}}}_0^{xy}\cdot\mathbf{n}_8 d\zeta = B_8, \\ \text{C4}: \dfrac{\partial\left(SI\left(\widetilde{\widetilde{B}}_x\right)\right)^2}{\partial\widetilde{\widetilde{a}}_5}=0, \\ \text{C5}: \dfrac{\partial\left(SI\left(\widetilde{\widetilde{B}}_y\right)\right)^2}{\partial\widetilde{\widetilde{b}}_3}=0, \end{cases} \tag{A.11}$$

subject to:

$$\begin{cases} \text{E1}: \widetilde{\widetilde{a}}_1+\widetilde{\widetilde{b}}_2=0, \\ \text{E2}: 2\widetilde{\widetilde{a}}_3+\widetilde{\widetilde{b}}_4=0, \\ \text{E3}: \widetilde{\widetilde{a}}_4+2\widetilde{\widetilde{b}}_5=0, \\ \text{E4}: n_{x,\ell_0^{-1}(l)}\left(\widetilde{\widetilde{a}}_0+\widetilde{\widetilde{a}}_1 x_{\ell_0^{-1}(l),m}+\widetilde{\widetilde{a}}_2 y_{\ell_0^{-1}(l),m}+\widetilde{\widetilde{a}}_3 x^2_{\ell_0^{-1}(l),m}+\widetilde{\widetilde{a}}_4 x_{\ell_0^{-1}(l),m}y_{\ell_0^{-1}(l),m}+\widetilde{\widetilde{a}}_5 y^2_{\ell_0^{-1}(l),m}\right) \\ \quad +n_{y,\ell_0^{-1}(l)}\left(\widetilde{\widetilde{b}}_0+\widetilde{\widetilde{b}}_1 x_{\ell_0^{-1}(l),m}+\widetilde{\widetilde{b}}_2 y_{\ell_0^{-1}(l),m}+\widetilde{\widetilde{b}}_3 x^2_{\ell_0^{-1}(l),m}+\widetilde{\widetilde{b}}_4 x_{\ell_0^{-1}(l),m}y_{\ell_0^{-1}(l),m}+\widetilde{\widetilde{b}}_5 y^2_{\ell_0^{-1}(l),m}\right) \\ \quad =\hat{a}_{\ell_0^{-1}(l)}-(1/2)\hat{c}_{\ell_0^{-1}(l)} \qquad \text{for } l=1,2, \\ \text{E5}: \Big[n_{x,\ell_0^{-1}(l')}\left(\widetilde{\widetilde{a}}_1\triangle x_{\ell_i^{-1}(l')}+\widetilde{\widetilde{a}}_2\triangle y_{\ell_0^{-1}(l')}+\widetilde{\widetilde{a}}_3 2x_{\ell_0^{-1}(l'),m}\triangle x_{\ell_0^{-1}(l')}\right. \\ \quad \left.+\widetilde{\widetilde{a}}_4(x_{\ell_0^{-1}(l'),m}\triangle y_{\ell_0^{-1}(l')}+y_{\ell_0^{-1}(l'),m}\triangle x_{\ell_0^{-1}(l')})+\widetilde{\widetilde{a}}_5 2y_{\ell_0^{-1}(l'),m}\triangle y_{\ell_0^{-1}(l')}\right) \\ \quad +n_{y,\ell_0^{-1}(l')}\left(\widetilde{\widetilde{b}}_{1'}\triangle x_{\ell_0^{-1}(l')}+\widetilde{\widetilde{b}}_2\triangle y_{\ell_i^{-1}(l')}+\widetilde{\widetilde{b}}_3 2x_{\ell_0^{-1}(l'),m}\triangle x_{\ell_0^{-1}(l')}\right. \\ \quad \left.+\widetilde{\widetilde{b}}_4(x_{\ell_0^{-1}(l'),m}\triangle y_{\ell_0^{-1}(l')}+y_{\ell_0^{-1}(l'),m}\triangle x_{\ell_0^{-1}(l')})+\widetilde{\widetilde{b}}_5 2y_{\ell_0^{-1}(l'),m}\triangle y_{\ell_0^{-1}(l')}\right)\Big] \\ \quad =\hat{b}_{\ell_0^{-1}(l')} \qquad \text{for } l'=1,2,3, \\ \text{E6}: \Big[n_{x,\ell_0^{-1}(l'')}\left(\widetilde{\widetilde{a}}_3\triangle x^2_{\ell_0^{-1}(l'')}+\widetilde{\widetilde{a}}_4\triangle x_{\ell_0^{-1}(l'')}\triangle y_{\ell_0^{-1}(l'')}+\widetilde{\widetilde{a}}_5\triangle y^2_{\ell_0^{-1}(l'')}\right) \\ \quad +n_{y,\ell_0^{-1}(l'')}\left(\widetilde{\widetilde{b}}_3\triangle x^2_{\ell_0^{-1}(l'')}+\widetilde{\widetilde{b}}_4\triangle x_{\ell_0^{-1}(l'')}\triangle y_{\ell_0^{-1}(l'')}+\widetilde{\widetilde{b}}_5\triangle y^2_{\ell_0^{-1}(l'')}\right)\Big] \\ \quad =(3/2)\hat{c}_{\ell_0^{-1}(l'')} \qquad \text{for } l''=1,2,3. \end{cases} \tag{A.12}$$

https://doi.org/10.4208/cicp.050814.040915a Published online by Cambridge University Press

Here function $SI()$ in Eqs. (A.11.C4) and (A.11.C5) is the smoothness measure of polynomial function defined in Eq. (A.6). Eqs. (A.11.C4) and (A.11.C5) are introduced to reduce variations in $\widetilde{\widetilde{a}}_5$ and $\widetilde{\widetilde{b}}_3$ in the reconstructed $\widetilde{\widetilde{\mathbf{B}}}_0^{xy}$. Eqs. (A.11.C1)-(A.11.C3) are for preserving the order of accuracy of the reconstructed $\widetilde{\widetilde{\mathbf{B}}}_0^{xy}$.

The linear constraint equations (A.12.E1)-(A.12.E3) are to satisfy the divergence-free condition $\nabla\cdot\widetilde{\widetilde{\mathbf{B}}}_0^{xy}=0$. The linear constraint equations (A.12.E4)-(A.12.E6) are to make sure that on each edge $\mathcal{L}_{\ell_0^{-1}(l)}, l=1,2,3$, the component of $\widetilde{\widetilde{\mathbf{B}}}_0^{xy}$ in the direction of edge unit normal $\mathbf{n}_{\ell_0^{-1}(l)}$ is the same as $\widetilde{B}_{n,\ell_0^{-1}(l)}$. Similar to the second-order accurate reconstruction, Eq. (A.12.E4) is only defined on two edges of $\mathcal{K}_i$. This is because that by the consistency condition (2.33), the edge length averaged value of $\widetilde{\widetilde{\mathbf{B}}}_0^{xy}(x,y)$ on the third edge also equates edge-length-averaged value of $\widetilde{B}_{n,\ell_0^{-1}(3)}$. Thus the reconstructed third-order accurate $\{\widetilde{\widetilde{\mathbf{B}}}_i^{xy}(x,y): i=1,\cdots\mathcal{N}\}$ has $\mathcal{C}^0$ continuous normal component on cell edges.

This finishes reconstructing the third-order accurate approximation to the magnetic field on triangular meshes.

References

[1] R. Abgrall. On essentially non-oscillatory schemes on unstructured meshes: analysis and implementation. *J. Comput. Phys.*, 144:45-58, 1994.

[2] J. Balbás and E. Tadmor. Non-oscillatory central scheme for one- and two-dimensional MHD equations. *SIAM J. Sci. Comput.*, 28(2):533-560, 2006.

[3] J. Balbás, E. Tadmor and C.-C. Wu. Non-oscillatory central scheme for one- and two-dimensional MHD equations: I. *J. Comput. Phys.*, 201:261-285, 2004.

[4] D.S. Balsara and D. Spicer. Maintaining pressure positivity in magnetohydrodynamic simulations. *J. Comput. Phys.*, 148:133-148, 1999.

[5] D.S. Balsara and D. Spicer. A Staggered mesh Algorithm Using High Order Godunov Fluxes to Ensure Solenoidal Magnetic Fields in Magnetohydrodynamic Simulations. *J. Comput. Phys.*, 149:270-292, 1999.

[6] D.S. Balsara. Divergence-free adaptive mesh refinement for magnetohydrodynamics. *J. Comput. Phys.*, 174:614-648, 2001.

[7] D.S. Balsara. Second-Order-Accurate Schemes for Magnetohydrodynamics with Divergence-Free Reconstruction. *The Astrophysical Journal Supplement Series*, 151:149-184, 2004.

[8] D.S. Balsara and J.-S. Kim. A Comparison between Divergence-Cleaning and Staggered-Mesh Formulations for Numerical Magnetohydrodynamics. *Astrophysical Journal*, 602(2):1079–1090, 2004.

[9] D.S. Balsara, T. Rumpf, M. Dumbser and C.D. Munz. Efficient, High Accuracy ADER-WENO Schemes for Hydrodynamics and Divergence-Free MHD. *J. Comput. Phys.*, 228:2480-2516, 2009.

[10] D.S. Balsara. Divergence-free reconstruction of magnetic fields and WENO schemes for magnetohydrodynamics. *J. Comput. Phys.*, 228(14):5040-5056, 2009.

https://doi.org/10.4208/cicp.050814.040915a Published online by Cambridge University Press

[11] D.S. Balsara. Multidimensional HLLE Riemann solver: Application to Euler and magnetohydrodynamic flows. *J. Comput. Phys.*, 229:1970-1993, 2010.
[12] D.S. Balsara, M. Dumbser and R. Abgrall. Multidimensional HLLC Riemann solver for unstructured meshes With application to Euler and MHD flows. *J. Comput. Phys.*, 231(22):7476-7503, 2014.
[13] D.S. Balsara. A two-dimensional HLLC Riemann solver for conservation laws: Application to Euler and magnetohydrodynamic flows. *J. Comput. Phys.*, 261:172-208, 2014.
[14] D.S. Balsara, C. Meyer, M. Dumbser, H. Du and Z.-L. Xu. Efficient Implementation of ADER Schemes for Euler and Magnetohydrodynamical Flows on Structured Meshes C Comparison with Runge-Kutta Methods. *J. Comput. Phys.*, 235(15):934, 2013.
[15] J.U. Brackbill and D.C. Barnes. The effect of nonzero $\nabla \cdot B$ on the numerical solution of the magnetohydrodynamic equations. *J. Comput. Phys.*, 35:426–430, 1980.
[16] S.H. Brecht, J.G. Lyon, J.A. Fedder and K. Hain. A simulation study of east-west IMF effets on the magnetosphere. *Geophysical Research Letters.*, 8:397-400, 1981.
[17] P. Cargo and G. Gallice. Roe Matrices for Ideal MHD and Systematic Construction of Roe Matrices for Systems of Conservation Laws. *J. Comput. Phys.*, 136:446-466, 1997.
[18] B. Cockburn, F. Li and C.-W. Shu. Locally divergence-free discontinuous Galerkin methods for the Maxwell equations. *J. Comput. Phys.*, 22-23:413-442, 2005.
[19] W. Dai and P.R. Woodward. On the divergence-free condition and conservation laws in numerical simulations for supersonic magnetohydrodynamic flows. *Astrophysical Journal*, 494:317–335, 1998.
[20] A. Dedner, F. Kemm, D. Kroner, C.D. Munz, T. Schnitzer and M. Wesenberg. Hyperbolic divergence-cleaning for the MHD equations. *J. Comput. Phys.*, 175:645, 2002.
[21] M. Dumbser and M. Käser. Arbitrary high order non-oscillatory finite volume schemes on unstructured meshes for linear hyperbolic systems. *J. Comput. Phys.*, 221:693–723, 2007.
[22] O. Friedrich. Weighted essentially non-oscillatory schemes for the interpolation of mean values on unstructured grids. *J. Comput. Phys.*, 144:194–212, 1998.
[23] T. Gardiner and J.M. Stone. An unsplit Godunov method for ideal MHD via constrained transport. *J. Comput. Phys.*, 205(2):509–539, 2005.
[24] A. Harten and S. Chakravarthy. Multi-dimensional ENO schemes for general geometries. *Technical Report* 91-76, ICASE, 1991.
[25] C. Hu and C.-W. Shu. Weighted essentially non-oscillatory schemes on triangular meshes. *J. Comput. Phys.*, 150:97–127, 1999.
[26] M. Käser and A. Iske. ADER schemes on adaptive triangular meshes for scalar conservation laws. *J. Comput. Phys.*, 205(2):486–508, 2005.
[27] D. Levy, G. Puppo and G. Russo. Central WENO schemes for hyperbolic systems of conservation laws. *ESAIM: Math. Modell. Numer. Anal.*, 33:547-571, 1999.
[28] F. Li, L. Xu and S. Yakovlev. Central discontinuous Galerkin methods for ideal MHD equations with the exactly divergence-free magnetic field. *J. Comput. Phys.*, 230(12):4828-4847, 2011.
[29] F. Li and C.-W. Shu. Locally divergence-free discontinuous Galerkin methods for MHD equations. *Journal of Scientific Computing*, 22-23:413-442, 2005.
[30] S. Li. High order central scheme on overlapping cells for magnetohydrodynamic flows with and without constrained transport method, *J. Comput. Phys.*, 227:7368–7393, 2008.
[31] P. Londrillo and L. DelZanna. On the divergence-free condition in Godunov-type schemes for ideal magnetohydrodynamics: the upwind constrained transport method, *J. Comput. Phys.*, 195:17–48, 2004.

https://doi.org/10.4208/cicp.050814.040915a Published online by Cambridge University Press

[32] T. Miyoshi and K. Kusano. A multi-state HLL approximate Riemann solver for ideal magnetohydrodynamics. *J. Comput. Phys.*, 208:315–344, 2005.
[33] S.A. Orszag and C.M. Tang. Small-scale structure of two-dimensional magnetohydrodynamic turbulence. *J. Fluid Mech.*, 90:129, 1979.
[34] K.G. Powell. An Approximate Riemann Solver for Magnetohydrodynamics. *Technical Report ICASE Report*, 94-24, ICASE, NASA Langley, 1994.
[35] P. L. Roe and D. S. Balsara. Notes on the eigensystem of magnetohydrodynamics. *SIAM Journal of applied Mathematics*, 56(1):57-67, 1996.
[36] D. Ryu and T.W. Jones. Numerical Magnetohydrodynamics in Astrophysics: Algorithm and Tests for One-Dimensional Flow. *Astrophysical J.*, 442:228–258, 1995.
[37] D. Ryu, F. Miniati, T.W. Jones and A. Frank. A divergence-free upwind code for multidimensional magnetohydrodynamic flows. *Astrophys. J.*, 509:244–255, 1998.
[38] J.M. Stone and M.L. Norman. ZEUS-2D: A radiation magnetohydrodynamics code for astrophysical flows in two space dimensions. II The magnetohydrodynamic algorithms and tests. *Astrophysical Journal Supplement Series.*, 80:791C818, 1992.
[39] C.-W. Shu and S. Osher. Efficient implementation of essentially non-scillatory capturing schemes. *J. Comput. Phys.*, 77:439-471, 1988.
[40] C.-W. Shu. Essentially non-oscillatory and weighted essentially non-oscillatory schemes for hyperbolic conservation laws. *In Advanced Numerical Approximation of Nonlinear Hyperbolic Equations, B. Cockburn, C. Johnson, C.-W. Shu and E. Tadmor (Editor: A. Quarteroni), Lecture Notes in Mathematics, Berlin. Springer*, 1697, 1998.
[41] T. Sonar. On the construction of essentially non-oscillatory finite volume approximations to hyperbolic conservation laws on general triangulations: polynomial recovery, accuracy and stencil selection. *Comput. Methods Appl. Mech. Engrg.*, 140:157-181, 1997.
[42] G. Tóth. The $\nabla \cdot B = 0$ constraint in shock-capturing magnetohydrodynamics codes. *J. Comput. Phys.*, 161:605-652, 2000.
[43] Z.-L. Xu and Y.-J. Liu and C.-W. Shu. Hierarchical reconstruction for discontinuous Galerkin methods on unstructured grids with a WENO type linear reconstruction and partial neighboring cells, *J. Comput. Phys.*, 228:2194–2212, 2009.
[44] K.S. Yee. Numerical solution of initial boundary value problems involving Maxwell's equatons in isotropic media. *IEEE Transactions on Antenna Propagation*, AP-14:302-307,1966.
[45] A.L. Zachary, A. Malagoli and P. Colella. A Higher-Order Godunov Method for Multidimensional Ideal Magnetohydrodynamics. *SIAM Journal on Scientific Computing*, 15(2):263–284, 1994.
[46] D.S. Balsara and M. Dumbser Multidimensional Riemann problem with self-similar internal structure. Part II Application to hyperbolic conservation laws on unstructured meshes Original. *J. Comput. Phys.*, 287:269-292, 2015.
[47] D.S. Balsara. Self-adjusting, positivity preserving high order schemes for hydrodynamics and magnetohydrodynamics. *J. Comput. Phys.*, 231(22):7504-7517,2012.
[48] Y. Cheng, F. Li, J. Qiu and L. Xu. Positivity-preserving DG and central DG methods for ideal MHD equations. *J. Comput. Phys.*, 238:255-280, 2013.

https://doi.org/10.4208/cicp.050814.040915a Published online by Cambridge University Press